ARTICLE

doi:10.1038/nature22397

Ensemble cryo–EM elucidates the mechanism of translation fidelity

Anna B. Loveland[1], Gabriel Demo[1], Nikolaus Grigorieff[2] & Andrei A. Korostelev[1]

Gene translation depends on accurate decoding of mRNA, the structural mechanism of which remains poorly understood. Ribosomes decode mRNA codons by selecting cognate aminoacyl–tRNAs delivered by elongation factor Tu (EF–Tu). Here we present high–resolution structural ensembles of ribosomes with cognate or near–cognate aminoacyl–tRNAs delivered by EF–Tu. Both cognate and near–cognate tRNA anticodons explore the aminoacyl–tRNA–binding site (A site) of an open 30S subunit, while inactive EF–Tu is separated from the 50S subunit. A transient conformation of decoding–centre nucleotide G530 stabilizes the cognate codon–anticodon helix, initiating step–wise 'latching' of the decoding centre. The resulting closure of the 30S subunit docks EF–Tu at the sarcin–ricin loop of the 50S subunit, activating EF–Tu for GTP hydrolysis and enabling accommodation of the aminoacyl–tRNA. By contrast, near–cognate complexes fail to induce the G530 latch, thus favouring open 30S pre–accommodation intermediates with inactive EF–Tu. This work reveals long–sought structural differences between the pre–accommodation of cognate and near–cognate tRNAs that elucidate the mechanism of accurate decoding.

Recognition of an mRNA codon by aminoacyl-tRNA occurs at the decoding centre in the A site of the small 30S ribosomal subunit. Aminoacyl-tRNA is delivered to the ribosome as a ternary complex with elongation factor Tu (EF-Tu) and GTP (EF-Tu•GTP•aminoacyl-tRNA). Non-cognate or near-cognate ternary complexes dissociate quickly, whereas cognate ternary complexes dissociate slowly and stimulate GTP hydrolysis by EF-Tu[1–8]. GTP hydrolysis releases EF-Tu•GDP, allowing aminoacyl-tRNA accommodation into the 50S A site for peptide-bond formation. EF-Tu-dependent aminoacyl-tRNA delivery, therefore, ensures the high fidelity of aminoacyl-tRNA selection[5,6,9].

The structural mechanism of aminoacyl-tRNA discrimination has been extensively studied, but key questions remain unresolved (reviewed in refs 10, 11). EF-Tu binds a highly conserved region of the large 50S ribosomal subunit called the sarcin–ricin loop (SRL), which prearranges the EF-Tu catalytic site for GTP hydrolysis[12–19]. The SRL lies more than 70 Å from the decoding centre, so how tRNA recognition activates the GTPase centre of EF-Tu remains unclear. Induced fit of the decoding centre—including universally conserved nucleotides G530, A1492 and A1493 of 16S rRNA, and A1913 of 23S rRNA—was proposed to provide the structural basis for tRNA recognition[1,20–22]. The mechanistic model focuses on A1492 and A1493, which flip out of the central 16S helix 44 to form A-minor interactions with the cognate codon–anticodon helix, thus monitoring the Watson–Crick geometry of the first and second base pairs[20]. This idea, however, has been questioned by observations that the decoding centre interacts similarly with mismatched codon–anticodon helices formed by fully accommodated near-cognate tRNAs[23]. Recent computational[24] and biochemical[25,26] studies arrive at diverse conclusions regarding the contribution of these A-minor interactions to decoding fidelity. It therefore remains undetermined what triggers the acceptance of cognate aminoacyl-tRNA at the decoding centre.

Biochemical and biophysical studies show that tRNA discrimination occurs before full accommodation. Decoding intermediates of the ribosome bound to EF-Tu•GTP•aminoacyl-tRNA result in rejection of near-cognate ternary complex or acceptance of the cognate ternary complex[2–6,8]. Thus, high-resolution structures of both cognate and near-cognate pre-accommodation intermediates would help to determine key questions such as how the decoding centre discriminates between cognate and near-cognate tRNAs, and how binding of the cognate aminoacyl-tRNA anticodon in the decoding centre is coordinated with GTPase activation by the SRL.

Here we use single-particle electron cryo-microscopy (cryo-EM) to visualize the binding of cognate or near-cognate ternary complexes to 70S ribosomes. Improved classification in FREALIGN[27,28] allows us to resolve several near-atomic-resolution structures in heterogeneous samples[29]. We identify six aminoacyl-tRNA decoding complexes at up to 3.2 Å resolution (Fig. 1, Extended Data Fig. 1), including five elusive pre-accommodation states not visualized previously (Fig. 1b, c, e–g). These structures report on three binding steps for ternary complex. Together, they reveal differences between cognate and near-cognate pre-accommodation states and suggest a mechanism of aminoacyl-tRNA discrimination by the ribosome.

Three states of cognate complex pre–accommodation

We visualized the dynamics of cognate Phe-tRNA^{Phe}•EF-Tu•GDPCP ternary complex on *Escherichia coli* 70S ribosomes programmed with mRNA encoding a phenylalanine UUC codon in the A site. A non-hydrolysable GTP analogue, GDPCP (guanosine-5′-[(β,γ)-methyleno]triphosphate), was used to capture aminoacyl-tRNA binding states before GTP hydrolysis and EF-Tu dissociation[15]. Maximum-likelihood classification[27,28] of 800,367 ribosome particles revealed three ribosome•tRNA•EF-Tu structures at 3.2–3.9 Å resolution: structures I, II and III (Fig. 1a–d, Extended Data Fig. 1, Extended Data Table 1). The high resolution of the maps allows detailed interpretation of interactions between the ribosome and ternary complex (Extended Data Figs 1–3). In structure I, the ternary complex binds the 30S subunit, but the anticodon does not base-pair with the codon (Figs 2, 3), nor does EF-Tu contact the 50S subunit (Fig. 4). In structure II, the anticodon base pairs with the codon, while EF-Tu remains distant from the 50S subunit. In structure III, the anticodon base-pairs with the codon, and EF-Tu contacts the SRL of the 50S subunit.

[1]RNA Therapeutics Institute, Department of Biochemistry and Molecular Pharmacology, University of Massachusetts Medical School, 368 Plantation Street, Worcester, Massachusetts 01605, USA. [2]Janelia Research Campus, Howard Hughes Medical Institute, 19700 Helix Drive, Ashburn, Virginia 20147, USA.

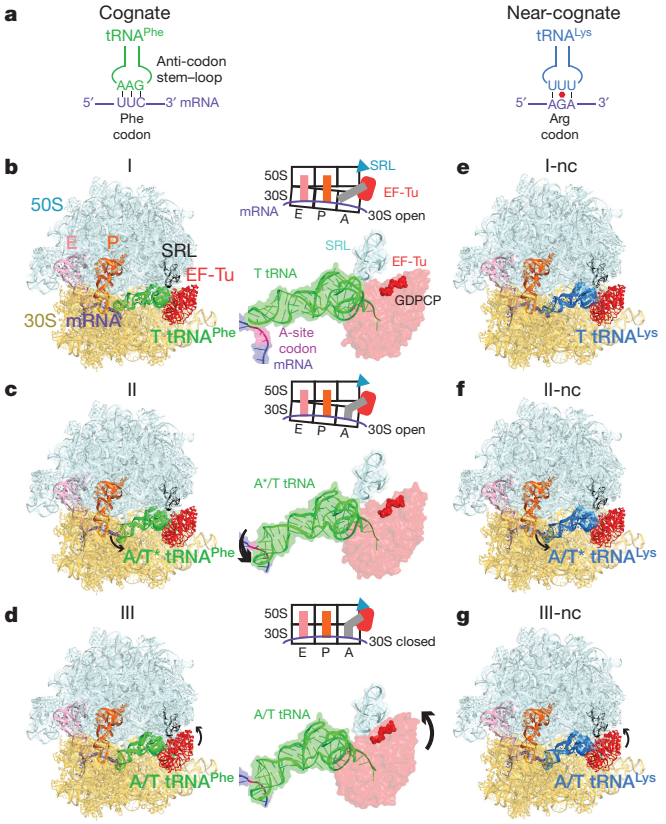

Figure 1 | Cryo-EM structures of cognate or near-cognate ternary complex on the 70S ribosome. a, Cognate (green) and near-cognate (blue) tRNA anticodons and A-site codons used in complexes. **b**, Structure I has cognate ternary complex on the ribosome with an open 30S subunit; the anticodon and codon are not paired. **c**, Structure II has cognate ternary complex on the ribosome with an open 30S subunit; the anticodon base-pairs with the codon. **d**, Structure III has cognate ternary complex on the ribosome with a closed 30S subunit; EF-Tu docks at the SRL. **e**–**g**, Structures I-nc, II-nc and III-nc with near-cognate ternary complex globally resemble the cognate structures.

Structures I and II reveal previously unobserved states of ternary-complex binding. These structures have an open 30S-domain conformation as in ribosomes without ternary complexes[20,21,30,31] or in stringent-response 70S•tRNA•RelA complexes[29]. In structure III, the distance from the 30S shoulder to the body closes by 4–5 Å (Fig. 2a, b, Extended Data Fig. 4a, b, Extended Data Table 2). The conformational change in the 30S subunit from structures I and II to structure III coincides with 30S 'domain closure', previously inferred from comparisons of 30S structures lacking or containing A-site tRNA anticodon stem–loops (ASLs)[20,30].

Multiple tRNA conformations sample the A site

Structures I and II reveal different conformations of EF-Tu-bound aminoacyl-tRNA, as the ASL interrogates the A site (Fig. 1b, c, Extended Data Fig. 4c). In structure I, the tRNA resembles the 'relaxed' conformation of ternary-complex tRNA (T tRNA) seen in crystal structures of isolated ternary complex[32]. The ASL of the tRNA reaches towards the peptidyl tRNA-binding site (P site) tRNA. The ASL tip is around 15 Å away from its codon-paired position (Fig. 2c, Extended Data Fig. 4d). In structure II, the ASL is kinked towards the A-site codon, forming three Watson–Crick codon–anticodon base pairs (Fig. 2d, Extended Data Fig. 4e). The tRNA conformation resembles that of A/T tRNA (A-site/ternary-complex tRNA) characterized in 70S structures with ternary complex[14,15,33–35]. Unlike in previous structures, however, the 30S subunit is open. We therefore distinguish this tRNA conformation as A*/T tRNA. Sub-classification of cryo-EM data revealed additional lower-resolution ASL conformations positioned between the T-tRNA and A*/T-tRNA states (Extended Data Fig. 4f, Supplementary Information).

In structure III, the tRNA adopts the A/T conformation[14,15,33–35]. From structures II to III, the tRNA binds deeper into the 30S A site without a substantial conformational change. The acceptor arm shifts by 7 Å towards the P-site tRNA as the elbow slides along the L11 stalk (Extended Data Fig. 5, Supplementary Information). The shift of the tRNA is in good agreement with single-molecule fluorescence resonance energy transfer (smFRET) studies that monitored step-wise binding of ternary complex[8] (Supplementary Information).

G530 triggers 'latching' of the decoding centre

The decoding centre provides the binding pocket for the ASL as the tRNA rearranges from the relaxed to the kinked conformation. Comparing structures I, II and III reveals new step-wise rearrangements of decoding-centre nucleotides in the presence of the ternary complex, suggesting that G530 at the tip of the 30S shoulder has a central role. In structure I, the decoding-centre nucleotides exhibit conformations found in ribosome structures with empty A sites[21,30,31] (Fig. 3a and Extended Data Fig. 6a, b). In particular, G530 is separated from the anticodon and helix 44. A1492 resides inside helix 44 and stacks with A1913 from helix 69 of 23S rRNA. A1493 bulges out from helix 44. Weak density suggests that the base does not stably interact with the A-site codon but is prearranged to bind the codon–anticodon helix. Thus, the decoding-centre nucleotides in structure I adopt the following conformations: G530 OFF, A1913 OFF, A1492 OFF and A1493 SEMI-ON.

Structure II reveals an intermediate position of G530. Strong density shows the nucleotide in the anti-conformation flipped out of the 530 loop and partially within the minor groove of the codon–anticodon helix (Fig. 3b, d, Extended Data Fig. 6c, d). G530 forms hydrogen bonds with the ribose groups of A35 (second nucleotide) of the tRNA anticodon and C3 of the mRNA codon (Fig. 5a). Therefore, G530 in the intermediate state (SEMI-ON) stabilizes the backbone of the codon–anticodon helix. Weak densities for A1492 and A1913 indicate conformational flexibility (ON/OFF). Strong density shows A1493 contacting

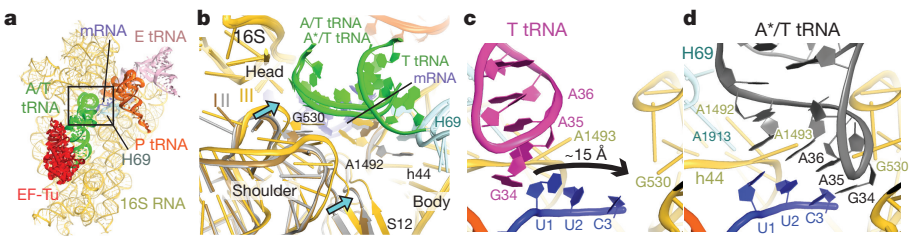

Figure 2 | Interactions of cognate ternary complex with the 30S subunit. **a**, 30S subunit shown from the inter-subunit interface with the decoding centre boxed. The 50S subunit (except for helix 69) and small-subunit proteins are omitted for clarity. **b**, Conformational differences among structures I, II and III suggest a domain-closure pathway. **c**, **d**, The anticodon in structure I is approximately 15 Å from the codon-paired position near G530 in structure II.

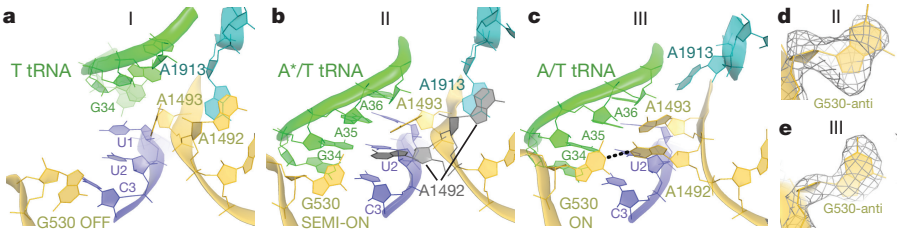

Figure 3 | Decoding-centre rearrangements in structures I–III. **a**, Disengaged decoding centre of structure I. **b**, In structure II, G530 adopts an intermediate position at the minor groove of the codon–anticodon helix. A1492 has partial occupancies inside and outside of helix 44 (grey). **c**, In structure III, G530 moves farther into the minor groove and hydrogen-bonds to A1492. **d**, **e**, Cryo-EM density (grey) showing G530 (yellow) in structures II (**d**) and III (**e**).

the minor groove of the first base pair of the codon–anticodon helix (A1493 ON).

Finally, the decoding-centre nucleotides in structure III adopt conformations seen in A-tRNA-bound and A/T-tRNA-bound structures[1,14,15,20–23,33] (G530/A1913/A1492/A1493 ON; Fig. 3c, e, Extended Data Fig. 6e, f). Relative to structure II, the 530 loop and protein S12 shift closer to A1493 and A1492, as G530 moves approximately 3 Å further into the minor groove of the codon–anticodon helix. This shift restructures the G530 hydrogen-bond network: G530 contacts the riboses of A35 and A36 of the anticodon (at the first and second base pairs) and the base of A1492 (Fig. 5b). Thus, G530 acts as a latch that fastens the codon–anticodon helix into the decoding centre, bringing the 530 loop of the 30S shoulder towards the body, resulting in 30S-domain closure.

30S-domain closure activates EF-Tu

Ternary complexes must bind the SRL to activate EF-Tu and hydrolyse GTP, releasing EF-Tu from aminoacyl-tRNA to allow aminoacyl-tRNA accommodation[12,13]. The SRL prearranges the catalytic His84 of EF-Tu to coordinate the catalytic water molecule[14,15]. Biochemical studies show that the SRL and His84 are indispensable for GTP hydrolysis and tRNA accommodation[16–18].

From structure I to structure III, EF-Tu progresses from the inactive GTPase state to the activated GTPase state. In all three structures, EF-Tu binds the shoulder of the 30S subunit at helices h5 and h15 of 16S rRNA and protein S12 (Extended Data Fig. 7). From structures I and II (30S open) to III (30S closed), the 30S shoulder moves towards the 50S subunit by around 4 Å, shifting the GTPase domain of EF-Tu by 8 Å to bind the SRL (Fig. 4). His84 binds the phosphate at A2662 of the SRL, near the terminal phosphate of GDPCP preparing for GTP hydrolysis (Fig. 4d, Extended Data Fig. 7f), as seen in the *Thermus thermophilus* 70S pre-accommodation structure[15]. Thus, our structures show that the decoding-centre-induced movement of the 30S shoulder activates EF-Tu.

Near-cognate ternary complex favours open 30S

We next asked whether near-cognate ternary complex has distinct pre-accommodation intermediates explaining discrimination during mRNA decoding. We repeated our experiment using a near-cognate 70S complex formed with $tRNA^{Lys}$ (UUU anticodon) and mRNA coding for arginine (AGA codon) in the A site, resulting in a G•U mismatch at the second position of the codon–anticodon helix (Fig. 1a, see Supplementary Information). A 572,417-particle dataset yielded three structures of EF-Tu-bound ribosomes at 3.8–4.0 Å resolution (Fig. 1e–g, Extended Data Figs 1–3, Extended Data Table 1). Overall, the near-cognate structures—structures I-nc, II-nc, and III-nc—resemble the cognate structures with aminoacyl-tRNA bound in the T (I-nc), A*/T (II-nc) and A/T (III-nc) states and the 30S in open (I-nc and II-nc) and closed (III-nc) conformations (Extended Data Figs 6j–n, 7g, Extended Data Table 2).

In structure II-nc, the decoding centre differs from that in the cognate structure II. Whereas G530 in structure II is clearly resolved in the anti-conformation and stabilizes the matched codon–anticodon helix (Fig. 5a, Extended Data Fig. 6g), G530 in structure II-nc is less resolved, and the density is more consistent with the syn-conformation (Fig. 5c, Extended Data Fig. 6k, o). The neighbouring nucleotides, however, are similarly well resolved in structures II and II-nc, indicating an ordered 530 loop (Extended Data Fig. 6d, l). G530 (OFF) is separated from the ASL, as the latter is shifted relative to the position of the cognate anticodon (Extended Data Fig. 6r, s, u, v). While the anticodon bases interact with the bases of the codon, the G•U mismatch and third base pair deviate from Watson–Crick conformations, thus shifting the anticodon (Fig. 5c, Extended Data Fig. 2o).

By contrast, in the 30S-closed structure III-nc, strong density reveals a canonical codon–anticodon helix with the G•U base pair in a tautomeric Watson–Crick-like conformation, similar to the U•A pair in structure III (Fig. 5b, d). The decoding-centre nucleotides in structure III-nc, including G530, are clearly resolved and adopt conformations similar to those in structure III (Extended Data Fig. 6m, n, p, q). Thus, G530 latching is coupled with the formation of the Watson–Crick codon–anticodon helix and coincides with domain closure.

Ternary complexes formed with $tRNA^{Phe}$ and $tRNA^{Lys}$ exhibit similar binding affinities to their respective codons[36,37] and accuracies of initial selection[38], allowing us to compare near-cognate and cognate samples. The distribution of ribosomes with cognate and near-cognate ternary complexes differed (Fig. 5e, f). Whereas cognate ternary complex bound to 34% of ribosomes, near-cognate ternary complex bound to 7% of ribosomes—despite assembling samples with 2.5-fold more near-cognate than cognate complex—consistent with the lower affinity of near-cognate ternary complex[1–8]. Moreover, the cognate complex predominantly samples the closed 30S state (87% of EF-Tu-bound ribosomes), but the near-cognate complex prefers the open 30S states (structures I-nc and II-nc, 67% of EF-Tu-bound ribosomes) (Fig. 5f). The identities and distributions of these structures are consistent with biochemical, structural and biophysical data (Supplementary Information). Thus, cognate ternary complexes favour an ordered decoding centre, closed 30S subunit, and activated EF-Tu, whereas the near-cognate complexes favour a disengaged decoding centre, open 30S subunit and inactive EF-Tu.

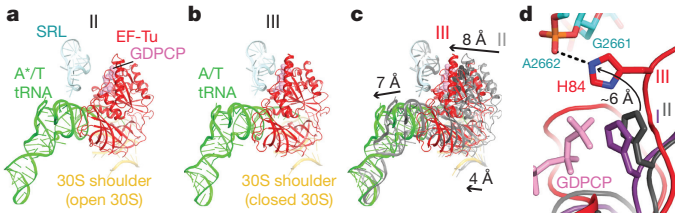

Figure 4 | Activation of EF-Tu GTPase from structures I–III. **a**, In structures I and II (shown), EF-Tu interacts with the open 30S subunit (shoulder helices 5 and 15, shown) but is distant from the SRL. **b**, In structure III, EF-Tu interacts with the closed 30S subunit and SRL. **c**, Movement of the 30S shoulder shifts EF-Tu towards the SRL from structure II (grey) to III (coloured). **d**, Catalytic residue His84 of EF-Tu is removed from the SRL in structures I (purple) and II (grey) but interacts with the SRL in structure III (coloured).

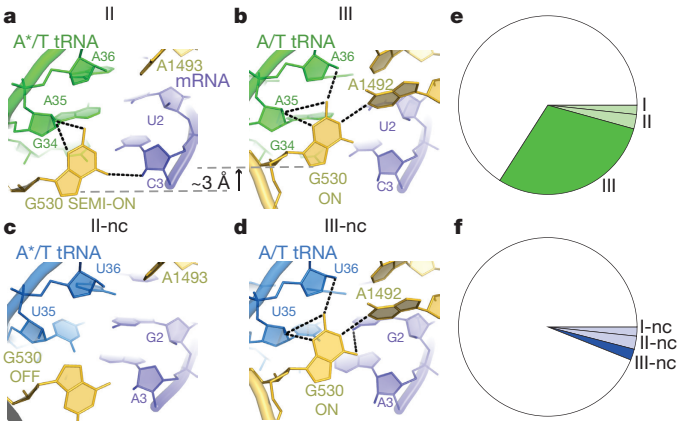

Figure 5 | Differences between the cognate and near-cognate structures. **a**, In structure II, G530 forms hydrogen bonds with the codon–anticodon backbone. **b**, In structure III, G530 moves approximately 3 Å, restructuring the hydrogen-bonding network. **c**, In structure II-nc, G530 does not stabilize the codon–anticodon helix. **d**, In structure III-nc, G530 stabilizes a Watson–Crick-like codon–anticodon helix. **e**, **f**, Distributions of ribosome particles in cognate (**e**) and near-cognate (**f**) structures.

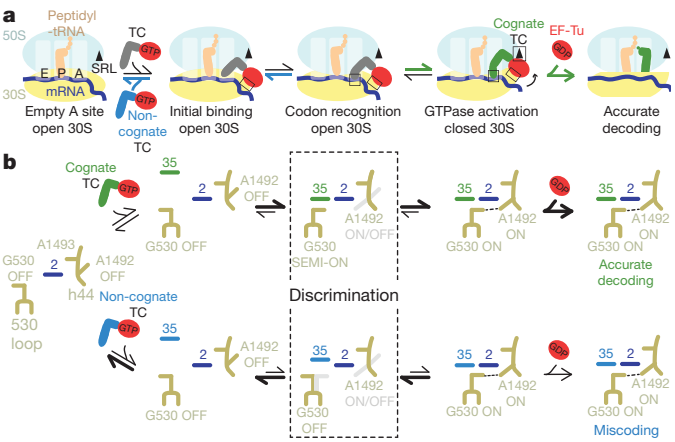

Figure 6 | Structural mechanism of initial aminoacyl-tRNA selection during mRNA decoding. Arrows indicate equilibrium shifts for cognate and near-cognate ternary complexes, inferred from biochemical studies and from particle distributions (this work). **a**, Structural mechanism of initial aminoacyl-tRNA selection. Boxes indicate step-wise interactions of ternary complex with the ribosome. **b**, Schematic of conformational changes in the decoding centre. TC, ternary complex.

A mechanism for accurate mRNA decoding

Our work reveals the elusive structures of pre-accommodation intermediates that coincide with the biochemically identified steps[4–6,8,12–15]: initial codon-independent binding of ternary complex (structures I and I-nc), codon recognition (structures II and II-nc) and GTPase activation (structures III and III-nc). The ensembles of cognate and near-cognate structures provide the structural basis for the initial selection of aminoacyl-tRNA (Fig. 6, Supplementary Video 1).

In the early step(s) of mRNA decoding, ternary complex binds the ribosome via EF-Tu at the 30S shoulder and the tRNA elbow at the L11 stalk (structure I or I-nc). The open 30S forces the EF-Tu GTPase domain away from the SRL. In the A site, the ASL samples the codon and the decoding centre (structures I/I-nc and II/II-nc). Formation of the matched codon–anticodon helix (structure II) is stabilized by interactions between the RNA backbone of the helix and G530 in an intermediate (SEMI-ON) conformation. Engagement of G530 is, thus, independent of the nucleotide identities of the Watson–Crick base pairs (Fig. 5), consistent with uniform affinities of distinct aminoacyl-tRNAs to their cognate codons[36,37]. Stabilization of G530 SEMI-ON, however, may be modulated by tRNA modifications at position 34 and magnesium (Supplementary Information, Extended Data Fig. 8). Bolstered by G530, ASL binding next to helices 44 and 69 destabilizes A1913 stacking on A1492 within helix 44. As A1913 interacts with the ASL, A1492 flips into the minor groove of the codon–anticodon helix, and G530 shifts to 'latch' the decoding centre, resulting in domain closure (structure III). The 30S shoulder moves towards the 50S subunit, docking EF-Tu at the SRL, arranging the EF-Tu active site for GTP hydrolysis. GTPase activation is a rate-limiting step of pre-accommodation[4,5], and is physically distinct from GTP hydrolysis[13]. Structures II and III suggest that GTPase activation results from 30S-domain closure pushing EF-Tu towards the SRL. Indeed, the antibiotic paromomycin, which stabilizes decoding-centre nucleotides G530, A1492 and A1493 in the 'ON' conformation favouring 30S-domain closure[1,20,22], accelerates GTPase activation for both cognate and near-cognate complexes[3]. The critical structural role of G530 is emphasized by mutational studies, which showed that G530 is indispensable for EF-Tu-dependent aminoacyl-tRNA binding[39], EF-Tu GTPase activation[40] and translation efficiency[41–43] (Supplementary Information).

Our structures show that domain closure requires Watson–Crick base pairing at the first two codon–anticodon positions (structures III and III-nc), as previously proposed based on 70S crystal structures with mismatched tRNA bound in the absence of EF-Tu[23]. The mismatched codon–anticodon helix in structure II-nc demonstrates that near-cognate tRNA is inefficient in stabilizing the G530 SEMI-ON state required to initiate 30S-domain closure. The high energetic cost of the Watson–Crick-like G•U base pair—which requires a keto-enol tautomerization[44]—shifts the conformational equilibrium towards the open 30S states, favouring departure of near-cognate ternary complex. Nevertheless, some near-cognate ternary complexes sample the less favourable Watson–Crick-like conformation and progress to domain closure and EF-Tu activation (structure III-nc). A small fraction of pre-accommodated near-cognate aminoacyl-tRNAs then escapes EF-Tu-independent proofreading[5,6,9,38], leading to rare miscoding.

Our work reveals a key role for G530 in decoding mRNA and demonstrates that accurate aminoacyl-tRNA selection is achieved by physical separation of EF-Tu from the SRL at early steps of pre-accommodation. We recently reported similar step-wise 30S-domain closure in the presence of deacyl-tRNA and RelA, demonstrating the universality of the tRNA acceptance mechanism[29]. While we were finalizing this manuscript, a cryo-EM study reported pre-activation states of SelB, a specialized elongation factor that binds an mRNA stem–loop structure and delivers a selenocysteine-tRNA to a UGA stop codon[45]. Although the resolution of the open-30S structures was limited to approximately 5 Å, and a Watson–Crick-paired codon–anticodon intermediate (similar to structure II) was not observed, the overall mechanism of SelB GTPase activation via the 30S-domain closure appears similar to that of EF-Tu. A lower-resolution (~8 Å) study of the eukaryotic elongation factor EF1A (a homologue of EF-Tu) bound to the 80S ribosome suggested that codon recognition and GTPase activation states differ in positions of aminoacyl-tRNA and the GTPase domain[46]. Together, these findings indicate that translation fidelity throughout all domains of life results from direct control of the GTPase by the decoding centre.

Online Content Methods, along with any additional Extended Data display items and Source Data, are available in the online version of the paper; references unique to these sections appear only in the online paper.

Received 15 December 2016; accepted 26 April 2017.
Published online 24 May 2017.

1. Ogle, J. M., Murphy, F. V., IV, Tarry, M. J. & Ramakrishnan, V. Selection of tRNA by the ribosome requires a transition from an open to a closed form. *Cell* **111,** 721–732 (2002).
2. Rodnina, M. V., Pape, T., Fricke, R., Kuhn, L. & Wintermeyer, W. Initial binding of the elongation factor Tu·GTP·aminoacyl-tRNA complex preceding codon recognition on the ribosome. *J. Biol. Chem.* **271,** 646–652 (1996).

3. Pape, T., Wintermeyer, W. & Rodnina, M. V. Conformational switch in the decoding region of 16S rRNA during aminoacyl-tRNA selection on the ribosome. *Nat. Struct. Mol. Biol.* **7,** 104–107 (2000).
4. Pape, T., Wintermeyer, W. & Rodnina, M. Induced fit in initial selection and proofreading of aminoacyl-tRNA on the ribosome. *EMBO J.* **18,** 3800–3807 (1999).
5. Gromadski, K. B. & Rodnina, M. V. Kinetic determinants of high-fidelity tRNA discrimination on the ribosome. *Mol. Cell* **13,** 191–200 (2004).
6. Gromadski, K. B., Daviter, T. & Rodnina, M. V. A uniform response to mismatches in codon–anticodon complexes ensures ribosomal fidelity. *Mol. Cell* **21,** 369–377 (2006).
7. Zhang, J., Ieong, K.-W., Johansson, M. & Ehrenberg, M. Accuracy of initial codon selection by aminoacyl-tRNAs on the mRNA-programmed bacterial ribosome. *Proc. Natl Acad. Sci. USA* **112,** 9602–9607 (2015).
8. Blanchard, S. C., Gonzalez, R. L., Kim, H. D., Chu, S. & Puglisi, J. D. tRNA selection and kinetic proofreading in translation. *Nat. Struct. Mol. Biol.* **11,** 1008–1014 (2004).
9. Ieong, K.-W., Uzun, Ü., Selmer, M. & Ehrenberg, M. Two proofreading steps amplify the accuracy of genetic code translation. *Proc. Natl Acad. Sci. USA* **113,** 13744–13749 (2016).
10. Voorhees, R. M. & Ramakrishnan, V. Structural basis of the translational elongation cycle. *Annu. Rev. Biochem.* **82,** 203–236 (2013).
11. Maracci, C. & Rodnina, M. V. Review: translational GTPases. *Biopolymers* **105,** 463–475 (2016).
12. Pape, T., Wintermeyer, W. & Rodnina, M. V. Complete kinetic mechanism of elongation factor Tu-dependent binding of aminoacyl-tRNA to the A site of the *E. coli* ribosome. *EMBO J.* **17,** 7490–7497 (1998).
13. Rodnina, M. V., Fricke, R., Kuhn, L. & Wintermeyer, W. Codon-dependent conformational change of elongation factor Tu preceding GTP hydrolysis on the ribosome. *EMBO J.* **14,** 2613–2619 (1995).
14. Schmeing, T. M. *et al.* The crystal structure of the ribosome bound to EF-Tu and aminoacyl-tRNA. *Science* **326,** 688–694 (2009).
15. Voorhees, R. M., Schmeing, T. M., Kelley, A. C. & Ramakrishnan, V. The mechanism for activation of GTP hydrolysis on the ribosome. *Science* **330,** 835–838 (2010).
16. Hausner, T. P., Atmadja, J. & Nierhaus, K. H. Evidence that the G2661 region of 23S rRNA is located at the ribosomal binding sites of both elongation factors. *Biochimie* **69,** 911–923 (1987).
17. Bilgin, N. & Ehrenberg, M. Mutations in 23 S ribosomal RNA perturb transfer RNA selection and can lead to streptomycin dependence. *J. Mol. Biol.* **235,** 813–824 (1994).
18. Daviter, T., Wieden, H.-J. & Rodnina, M. V. Essential role of histidine 84 in elongation factor Tu for the chemical step of GTP hydrolysis on the ribosome. *J. Mol. Biol.* **332,** 689–699 (2003).
19. Moazed, D., Robertson, J. M. & Noller, H. F. Interaction of elongation factors EF-G and EF-Tu with a conserved loop in 23S RNA. *Nature* **334,** 362–364 (1988).
20. Ogle, J. M. *et al.* Recognition of cognate transfer RNA by the 30S ribosomal subunit. *Science* **292,** 897–902 (2001).
21. Jenner, L., Demeshkina, N., Yusupova, G. & Yusupov, M. Structural rearrangements of the ribosome at the tRNA proofreading step. *Nat. Struct. Mol. Biol.* **17,** 1072–1078 (2010).
22. Selmer, M. *et al.* Structure of the 70S ribosome complexed with mRNA and tRNA. *Science* **313,** 1935–1942 (2006).
23. Demeshkina, N., Jenner, L., Westhof, E., Yusupov, M. & Yusupova, G. A new understanding of the decoding principle on the ribosome. *Nature* **484,** 256–259 (2012).
24. Zeng, X., Chugh, J., Casiano-Negroni, A., Al-Hashimi, H. M. & Brooks, C. L., III. Flipping of the ribosomal A-site adenines provides a basis for tRNA selection. *J. Mol. Biol.* **426,** 3201–3213 (2014).
25. Schrode, P., Huter, P., Clementi, N. & Erlacher, M. Atomic mutagenesis at the ribosomal decoding site. *RNA Biol.* **14,** 104–112 (2016).
26. Khade, P. K., Shi, X. & Joseph, S. Steric complementarity in the decoding center is important for tRNA selection by the ribosome. *J. Mol. Biol.* **425,** 3778–3789 (2013).
27. Lyumkis, D., Brilot, A. F., Theobald, D. L. & Grigorieff, N. Likelihood-based classification of cryo-EM images using FREALIGN. *J. Struct. Biol.* **183,** 377–388 (2013).
28. Grigorieff, N. Frealign: an exploratory tool for single-particle cryo-EM. *Methods Enzymol.* **579,** 191–226 (2016).
29. Loveland, A. B. *et al.* Ribosome•RelA structures reveal the mechanism of stringent response activation. *eLife* **5,** e17029 (2016).
30. Wimberly, B. T. *et al.* Structure of the 30S ribosomal subunit. *Nature* **407,** 327–339 (2000).
31. Schuwirth, B. S. *et al.* Structures of the bacterial ribosome at 3.5 Å resolution. *Science* **310,** 827–834 (2005).
32. Nissen, P. *et al.* Crystal structure of the ternary complex of Phe-tRNAPhe, EF-Tu, and a GTP analog. *Science* **270,** 1464–1472 (1995).
33. Fischer, N. *et al.* Structure of the *E. coli* ribosome-EF-Tu complex at <3 Å resolution by Cs-corrected cryo-EM. *Nature* **520,** 567–570 (2015).
34. Valle, M. *et al.* Cryo-EM reveals an active role for aminoacyl-tRNA in the accommodation process. *EMBO J.* **21,** 3557–3567 (2002).
35. Stark, H. *et al.* Visualization of elongation factor Tu on the *Escherichia coli* ribosome. *Nature* **389,** 403–406 (1997).
36. Ledoux, S. & Uhlenbeck, O. C. Different aa-tRNAs are selected uniformly on the ribosome. *Mol. Cell* **31,** 114–123 (2008).
37. Fahlman, R. P., Dale, T. & Uhlenbeck, O. C. Uniform binding of aminoacylated transfer RNAs to the ribosomal A and P sites. *Mol. Cell* **16,** 799–805 (2004).
38. Zhang, J., Ieong, K.-W., Mellenius, H. & Ehrenberg, M. Proofreading neutralizes potential error hotspots in genetic code translation by transfer RNAs. *RNA* **22,** 896–904 (2016).
39. Powers, T. & Noller, H. F. Evidence for functional interaction between elongation factor Tu and 16S ribosomal RNA. *Proc. Natl Acad. Sci. USA* **90,** 1364–1368 (1993).
40. Cochella, L., Brunelle, J. L. & Green, R. Mutational analysis reveals two independent molecular requirements during transfer RNA selection on the ribosome. *Nat. Struct. Mol. Biol.* **14,** 30–36 (2007).
41. Abdi, N. M. & Fredrick, K. Contribution of 16S rRNA nucleotides forming the 30S subunit A and P sites to translation in *Escherichia coli*. *RNA* **11,** 1624–1632 (2005).
42. Santer, M. *et al.* Functional effects of a G to U base change at position 530 in a highly conserved loop of *Escherichia coli* 16S RNA. *Biochemistry* **32,** 5539–5547 (1993).
43. Taliaferro, D. L. & Farabaugh, P. J. Testing constraints on rRNA bases that make nonsequence-specific contacts with the codon-anticodon complex in the ribosomal A site. *RNA* **13,** 1279–1286 (2007).
44. Westhof, E. Isostericity and tautomerism of base pairs in nucleic acids. *FEBS Lett.* **588,** 2464–2469 (2014).
45. Fischer, N. *et al.* The pathway to GTPase activation of elongation factor SelB on the ribosome. *Nature* **540,** 80–85 (2016).
46. Budkevich, T. V. *et al.* Regulation of the mammalian elongation cycle by subunit rolling: a eukaryotic-specific ribosome rearrangement. *Cell* **158,** 121–131 (2014).

Supplementary Information is available in the online version of the paper.

Acknowledgements We thank A. Park for help with preparing ribosome complexes; C. Xu and M. Rigney for help with preparing and screening cryo-EM grids at the cryo-EM facility at Brandeis University; Z. Yu, C. Hong, A. Rohou and R. Diaz-Avalos for data collection at Janelia Research Campus; D. Ermolenko for sharing an EF-Tu-overexpression plasmid and helpful comments on the manuscript; A. Korennykh, D. Conte Jr and members of the Korostelev laboratories for comments on the manuscript. This study was supported by NIH Grants R01 GM106105 and GM107465 (to A.A.K.) and P01 GM62580 (to N.G.). A.B.L. performed this work as a Howard Hughes Medical Institute Fellow of the Helen Hay Whitney Foundation.

Author Contributions A.B.L., N.G. and A.A.K. designed the project; A.B.L. prepared ribosome complexes, collected and analysed cryo-EM data; G.D. assisted with protein purification and prepared ribosomes; N.G. and A.A.K. oversaw cryo-EM data processing; A.B.L. and A.A.K. built and refined structural models; A.B.L. and A.A.K. wrote the manuscript; all authors contributed to manuscript finalization.

Author Information Reprints and permissions information is available at www.nature.com/reprints. The authors declare no competing financial interests. Readers are welcome to comment on the online version of the paper. Publisher's note: Springer Nature remains neutral with regard to jurisdictional claims in published maps and institutional affiliations. Correspondence and requests for materials should be addressed to A.A.K. (andrei.korostelev@umassmed.edu).

Reviewer Information *Nature* thanks M. Erlacher, R. Gillet and the other anonymous reviewer(s) for their contribution to the peer review of this work.

METHODS

No statistical methods were used to predetermine sample size. The experiments were not randomized, and investigators were not blinded to allocation during experiments and outcome assessment.

Preparation of *E. coli* 70S ribosome bound with the cognate or near-cognate ternary complex. *Escherichia coli* EF-Tu (*tufB* gene) with a C-terminal hexahistidine tag was overexpressed and purified essentially as described[47]. The crude *E. coli* EF-Tu-containing lysate was passed through a His-Trap-HP column. The column was washed with wash buffer (50 mM HEPES-KOH, pH 7.5, 60 mM ammonium chloride, 7 mM magnesium chloride, 15 mM imidazole, 500 mM KCl, 5% glycerol) and EF-Tu was eluted with a linear gradient of wash buffer mixed with elution buffer (50 mM HEPES-KOH, pH 7.5, 60 mM ammonium chloride, 7 mM magnesium chloride, 250 mM imidazole, 5% glycerol). The purity of EF-Tu in eluted fractions was assessed by SDS–PAGE and agarose gel electrophoresis. The purest fractions (>95%) were concentrated and exchanged into EF-Tu storage buffer (50 mM HEPES-KOH, pH 7.5, 60 mM ammonium chloride, 7 mM magnesium chloride, 10% glycerol, 6 mM β-mercaptoethanol, 20 μM GDP), flash-frozen in liquid nitrogen, and stored at −80 °C.

30S and 50S ribosomal subunits were prepared from MRE600 *E. coli* as described previously[48,49] and stored in buffer A (20 mM Tris, pH 7, 10.5 mM $MgCl_2$, 100 mM NH_4Cl, 0.5 mM EDTA, 6 mM β-mercaptoethanol) at −80 °C. S100 extract was prepared as described[50]. $tRNA^{fMet}$, $tRNA^{Phe}$, and $tRNA^{Lys}$ (ChemBlock) were charged with their cognate amino acids using the S100 extract and the aminoacylation of tRNAs was confirmed by polyacrylamide gel electrophoresis as described[51]. mRNA containing the Shine–Dalgarno sequence and a linker to place the AUG codon in the P site and the desired codon in the A site were synthesized by IDT DNA and had the following sequences: Phe cognate complex: GGCAAGGAGGUAAAAAUGUUCAAAAAA; Lys near-cognate complex: GGCAAGGAGGUAAAAAUGAGAAAAAAA (see Supplementary Information).

The 70S•mRNA•fMet-$tRNA^{fMet}$•EF-Tu•GDPCP•aminoacyl-tRNA complexes were prepared as follows. Heat-activated (42 °C) 30S ribosomal subunits (4 μM) were mixed with 50S ribosomal subunits (4 μM) and with the cognate or near-cognate mRNA (20 μM) (all final concentrations) in reaction buffer (20 mM HEPES-KOH, pH 7.5, 20 mM magnesium chloride, 150 mM ammonium chloride, 2 mM spermidine, 0.1 mM spermine, 6 mM β-mercaptoethanol) for 45 min at 37 °C. A twofold molar excess of fMet-$tRNA^{fMet}$ was added to the ribosomal subunits and incubated for 5 min at 37 °C, resulting in the 70S•mRNA•fMet-$tRNA^{fMet}$ complexes. To prepare the isolated ternary complex with Phe-$tRNA^{Phe}$, 2 μM EF-Tu was pre-incubated with 1 mM GDPCP (Jena Bioscience) for 5 min at 37 °C and then was supplemented with 2 μM Phe-$tRNA^{Phe}$ and incubated for 1 min at 37 °C. For the $tRNA^{Lys}$ ternary complex, 2.5 μM EF-Tu was pre-incubated with 1 mM GDPCP (Jena Bioscience) for 5 min at 37 °C and then was supplemented with 2.5 μM Lys-$tRNA^{Lys}$ and incubated for 1 min at 37 °C. Subsequently, the ternary complexes were chilled on ice and mixed with the 70S•mRNA•fMet-$tRNA^{fMet}$ complexes resulting in the following concentrations for the cognate complex: 250 nM 50S; 250 nM 30S; 1.25 μM mRNA; 500 nM fMet-$tRNA^{fMet}$; 1 μM EF-Tu; 500 μM GDPCP, and 1 μM Phe-$tRNA^{Phe}$; for the near-cognate complex: 125 nM 50S; 125 nM 30S; 625 nM mRNA; 250 nM fMet-$tRNA^{fMet}$; 1.25 μM EF-Tu; 500 μM GDPCP, and 1.25 μM Lys-$tRNA^{Lys}$. The complexes were equilibrated on ice for at least 5 min before application to cryo-EM grids.

Grid preparation. Holey-carbon grids (C-flat 1.2-1.3, Protochips) were coated with a thin layer of carbon and glow discharged with 20 mA with negative polarity for 45 s in an EMITECH K100X glow discharge unit. 2 μl of 70S•ternary complex sample was applied to each grid. After a 10-s incubation, the grids were blotted for 2–4 s at 4 °C and ~95% humidity, and plunged into liquid ethane using a CP3 cryo plunger (Gatan Inc.).

Electron microscopy. Data for the cognate complex and near-cognate complex were collected on a Titan Krios electron microscope (FEI) operating at 300 kV and equipped with K2 Summit direct electron detector (Gatan Inc.) using 0.5–2.2-μm underfocus. For the cognate complex, a dataset of 800,367 particles from 3,028 videos was collected automatically using SerialEM[52]. 50 frames per video were collected at 1 e^- $Å^{-2}$ per frame for a total exposure of 50 e^- $Å^{-2}$ on the sample. For the near-cognate complex, a dataset of 572,417 particles from 1,773 videos of 30 frames each was collected. The videos for the near-cognate complex were taken with 1 e^- $Å^{-2}$ per frame for a total exposure of 30 e^- $Å^{-2}$ on the sample. For both datasets, the super-resolution pixel size was 0.82 Å on the sample.

Image processing. Particles were extracted from aligned video sums as follows. Videos were processed using IMOD[53] to decompress frames and apply the gain reference. Videos were drift-corrected using unblur[54]. Magnification anisotropy of the video sums was corrected with mag_distortion_estimate and mag_distortion_correct[55]. CTFFIND3[56] was used to determine defocus values. Particles were automatically picked from 10× binned images using Signature[57] with a ribosome reference (18 representative reprojections of the EM databank map 1003[58], which was low-pass filtered to 50 Å). 480 × 480-pixel boxes with particles were extracted from super-resolution-aligned and magnification-anisotropy-corrected images, and the stack and FREALIGN parameter file were assembled in EMAN2[59]. To speed up processing, binned image stacks were prepared using resample.exe, which is part of the FREALIGN distribution[27].

High-resolution map refinement and reconstruction. FREALIGN version 9 (versions 9.07–9.11) was used for all steps of refinement and reconstruction[27] (Extended Data Fig. 1). A 6× binned image stack was initially aligned to a ribosome reference (EM databank map 1003; ref. 58) using three rounds of mode 3 (global search) alignment, including data in the resolution range from 300 Å to 30 Å. Next, the 2× binned, and later the unbinned image stacks were successively aligned against the common reference using mode 1 (local refinement), including data up to a high-resolution limit (6 Å for the cognate ternary complex or 8 Å for near-cognate ternary complex), whereupon the resolution of the common reference stopped improving. Subsequently, the refined parameters were used for classification of 4× binned stacks into 6 classes in 50 rounds using a spherical (60-Å radius) focus mask around EF-Tu and A/T tRNA, including resolutions from 300 Å to 8 Å during classification. This procedure yielded three EF-Tu-containing classes for the cognate complex and one for the near-cognate complex (Extended Data Fig. 1).

Further processing of the cognate complex was as follows. The structure III map at 3.2 Å resolution was obtained from the 6-model classification described above at 1× binning. A related map, structure IIIb, also had a closed 30S conformation and activated EF-Tu at the SRL, but a disordered L11 stalk. This class consisted of 72,533 particles and was not used for structure modelling and refinements. Finally, 50,667 particles belonging to the open-30S class were extracted using merge_classes.exe, including particles with >50% occupancy and scores >0. The resulting substack was subjected to further classification with a focused mask (30 Å radius) around the decoding centre. Using three classes separated structure I and structure II from a third class in which the anticodon was disordered. The final maps for the structures I and II were prepared from these classes, using 50% of particles with highest scores.

Further processing of the near-cognate complex proceeded as follows. 37,341 particles belonging to the single class bound with EF-Tu from the 6-model classification described above, were extracted using merge_classes.exe using thresholds of >90% occupancy and scores >10. The particles were classified again for 50 rounds using the same 60-Å-wide focus mask around EF-Tu and A/T tRNA, including resolutions from 300 Å to 8 Å during classification. This classification separated the near-cognate GTPase-activated state (structure III-nc) from two maps with an open 30S subunit. Particles belonging to structure III-nc were extracted using merge_classes.exe with thresholds of >75% occupancy and scores >10, and 50% of them with the highest score were used to prepare the final structure III-nc map. Particles belonging to the classes with the open 30S subunit were extracted using merge_classes.exe with thresholds of >75% occupancy and scores >10. The resulting substack of 23,078 particles was subjected to a 2-model classification with a focused mask (30-Å radius) around the decoding centre. The final maps for structures I-nc and II-nc were prepared from these classes, using 50% of particles with highest scores.

We report the percentages of the particles that belong to structures I, II or III or structures I-nc, II-nc, or IIInc in Fig. 5e, f. The percentages were calculated using all particles assigned to the corresponding classes shown in Extended Data Fig. 1 (structure III comprises particles assigned to both 30S-domain-closed classes III and IIIb, which only differ in the L11 stalk occupancy, as described above).

The maps used for structure refinements were sharpened by applying negative B-factors of up to −100 $Å^2$ using bfactor.exe (included with the FREALIGN distribution[27]). FSC curves were calculated by FREALIGN for even and odd particle half-sets. frealign_calc_stats was used to derive the number of particles assigned to each class. Blocres was used to assess local resolution of unfiltered and unmasked volumes using a box size of 60 pixels, step size of 10 pixels, and resolution criterion of FSC value at 0.143 (ref. 60).

Model building and refinement. The high-resolution cryo-EM structure of the 70S•tRNA•EF-Tu•GDP•kirromycin complex (PDB code 5AFI)[33], excluding EF-Tu, A/T-, P- and E-site tRNAs, was used as a starting model for structure refinements. The starting structural models for fMet-$tRNA^{fMet}$ in the P and E sites were adopted from the 70S•RF2•tRNA crystal structure[61]. We could not distinguish the identity of E-site tRNA ($tRNA^{fMet}$ or $tRNA^{Phe}$ for cognate complex or $tRNA^{fMet}$ or $tRNA^{Lys}$ for near-cognate complex) owing to lower than average resolution of this part of the cryo-EM maps, probably due to conformational flexibility suggested by further classification. Since $tRNA^{fmet}$ was used in the absence of EF-Tu and is likely to bind the E site upon deacylation, we modelled the E-site tRNA as $tRNA^{fMet}$. The starting model for A/T Phe-$tRNA^{Phe}$ in structures II and III was taken from PDB code 5AFI

(ref. 33). The starting model for Phe-tRNA^{Phe} in structure I was from the crystal structure of the isolated *Thermus aquaticus* ternary complex (PDB code 1TTT)[32]. For the near-cognate structures, the starting model for Lys-tRNA^{Lys} was from the crystal structure of the ribosome with a near-cognate tRNA^{Lys} in the A site (PDB code 5IB8)[62]. The *T. aquaticus* ternary complex (PDB code 1TTT)[32] was used for homology modelling of *E. coli* EF-Tu using SWISS-PROT[63] and deriving the initial structure of GDPCP. A homology model was similarly created for *E. coli* L1 using the crystal structure of the isolated *T. thermophilus* L1 stalk (PDB code 3U4M)[64].

All structures were domain-fitted using Chimera[65] and refined using real-space simulated-annealing refinement using RSRef[66,67] against corresponding maps. Atomic electron scattering factors[68] were used during refinement. Local structural elements that differed between structures, such as the decoding centre, were manually fitted into cryo-EM maps before refinement. Refinement parameters, such as the relative weighting of stereochemical restraints and experimental energy term, were optimized to produce the optimal structure stereochemistry, real-space correlation coefficient and R-factor, which report on the fit of the model to the map[69]. Secondary-structure restraints, comprising hydrogen-bonding restraints for ribosomal proteins and base-pairing restraints for RNA molecules were used as described[70]. The structures were next refined using phenix.real_space_refine[71] followed by a round of refinement in RSRef applying harmonic restraints to preserve protein backbone geometry[66,67]. Ions were modelled as Mg^{2+} in structure III, filling the difference-map peaks (using CNS)[72] residing next to oxygen atoms. Phenix was used to refine B-factors of the models against their respective maps[71]. The resulting structural models have good stereochemical parameters, characterized by low deviation from ideal bond lengths and angles and agree closely with the corresponding maps as indicated by high correlation coefficients and low real-space R factors (Extended Data Table 1). Structure quality was validated using MolProbity[73].

The cryo-EM maps for structure I and structure II-nc did not allow unambiguous visual assignment of the G530 conformation. To interpret a predominant conformation, we prepared two ribosome models with G530 in the alternative conformations, 'syn' and 'anti', and refined the complete ribosome structures independently against corresponding maps. Following the refinements, a preferred fit was assessed based on the local real-space correlation coefficient (calculated only for G530 non-hydrogen atoms). The local correlation coefficient in structure I suggests that G530-syn and G530-anti fit nearly equally well (correlation coefficient = 0.67 versus 0.66, respectively, Extended Data Fig. 6b). The local correlation coefficient in structure II-nc suggests a better fit for G530-syn (correlation coefficient = 0.63), whereas a refined G530-anti yields the moderately lower correlation coefficient of 0.57. In structure II, whose density unambiguously shows G530-anti (Extended Data Fig. 8d, g), this preferred conformation yields a correlation coefficient value of 0.71, whereas a refined G530-syn fits poorly and exhibits a correlation coefficient of 0.44.

Figures were prepared in Chimera and Pymol[65,74].

Calculation of distance differences using smFRET data. We used published results to estimate the real-time change in distance between accommodating aminoacyl-tRNA and P-site-bound tRNA during EF-Tu-mediated tRNA accommodation. An absolute distance between two labelled residues in smFRET experiment is difficult to measure, but distance differences can be derived from relative changes between two FRET efficiency values[75]. A low-FRET state of 0.35 in ref. 8 or 0.33 in ref. 76 and mid-FRET state of 0.5 (ref. 8) or 0.43 (ref. 76) were reported during aminoacyl-tRNA accommodation when residue 47 of the accommodating tRNA was labelled with acceptor dye and residue 8 of P-site tRNA was labelled with donor dye. Using the equation in ref. 75 to deduce distance differences from FRET efficiencies and assuming R_0 of 55 Å for the Cy3/Cy5 FRET pair, we calculate that the accommodating tRNA is 4–6 Å farther from P-site tRNA in the low-FRET state than in the mid-FRET state.

Data availability. The models generated and analysed during the current study are available from the RCSB Protein Data Bank (PDB) under the accession codes 5UYK (structure I), 5UYL (structure II), 5UYM (structure IIII), 5UYN (structure I-nc), 5UYP (structure II-nc) and 5UYQ (structure III-nc). The cryo-EM maps used to generate models are available from the Electron Microscopy Data Bank (EMDB) under the accession codes EMBD-8615 (structure I), EMBD-8616 (structure II), EMBD-8617 (structure IIII), EMBD-8618 (structure I-nc), EMBD-8619 (structure II-nc) and EMBD-8620 (structure III-nc). All other data are available from the corresponding author upon reasonable request.

47. Brilot, A. F., Korostelev, A. A., Ermolenko, D. N. & Grigorieff, N. Structure of the ribosome with elongation factor G trapped in the pretranslocation state. *Proc. Natl Acad. Sci. USA* **110,** 20994–20999 (2013).
48. Moazed, D. & Noller, H. F. Interaction of tRNA with 23S rRNA in the ribosomal A, P, and E sites. *Cell* **57,** 585–597 (1989).
49. Moazed, D. & Noller, H. F. Transfer RNA shields specific nucleotides in 16S ribosomal RNA from attack by chemical probes. *Cell* **47,** 985–994 (1986).
50. Traub, P., Mizushima, S., Lowry, C. V. & Nomura, M. in *Nucleic Acids and Protein Synthesis, Part C* (eds Kaplan, N. & Colowick, N.) Vol. 20, 391–407 (Academic Press, 1971).
51. Walker, S. E. & Fredrick, K. Preparation and evaluation of acylated tRNAs. *Methods* **44,** 81–86 (2008).
52. Mastronarde, D. N. Automated electron microscope tomography using robust prediction of specimen movements. *J. Struct. Biol.* **152,** 36–51 (2005).
53. Kremer, J. R., Mastronarde, D. N. & McIntosh, J. R. Computer visualization of three-dimensional image data using IMOD. *J. Struct. Biol.* **116,** 71–76 (1996).
54. Grant, T. & Grigorieff, N. Measuring the optimal exposure for single particle cryo-EM using a 2.6 Å reconstruction of rotavirus VP6. *eLife* **4,** e06980 (2015).
55. Grant, T. & Grigorieff, N. Automatic estimation and correction of anisotropic magnification distortion in electron microscopes. *J. Struct. Biol.* **192,** 204–208 (2015).
56. Mindell, J. A. & Grigorieff, N. Accurate determination of local defocus and specimen tilt in electron microscopy. *J. Struct. Biol.* **142,** 334–347 (2003).
57. Chen, J. Z. & Grigorieff, N. SIGNATURE: a single-particle selection system for molecular electron microscopy. *J. Struct. Biol.* **157,** 168–173 (2007).
58. Gabashvili, I. S. *et al.* Solution structure of the *E. coli* 70S ribosome at 11.5 Å resolution. *Cell* **100,** 537–549 (2000).
59. Tang, G. *et al.* EMAN2: an extensible image processing suite for electron microscopy. *J. Struct. Biol.* **157,** 38–46 (2007).
60. Cardone, G., Heymann, J. B. & Steven, A. C. One number does not fit all: mapping local variations in resolution in cryo-EM reconstructions. *J. Struct. Biol.* **184,** 226–236 (2013).
61. Korostelev, A. *et al.* Crystal structure of a translation termination complex formed with release factor RF2. *Proc. Natl Acad. Sci. USA* **105,** 19684–19689 (2008).
62. Rozov, A., Westhof, E., Yusupov, M. & Yusupova, G. The ribosome prohibits the G•U wobble geometry at the first position of the codon-anticodon helix. *Nucleic Acids Res.* **44,** 6434–6441 (2016).
63. Bairoch, A., Boeckmann, B., Ferro, S. & Gasteiger, E. Swiss-Prot: juggling between evolution and stability. *Brief. Bioinform.* **5,** 39–55 (2004).
64. Tishchenko, S. *et al.* High-resolution crystal structure of the isolated ribosomal L1 stalk. *Acta Crystallogr. D* **68,** 1051–1057 (2012).
65. Pettersen, E. F. *et al.* UCSF Chimera--a visualization system for exploratory research and analysis. *J. Comput. Chem.* **25,** 1605–1612 (2004).
66. Korostelev, A., Bertram, R. & Chapman, M. S. Simulated-annealing real-space refinement as a tool in model building. *Acta Crystallogr. D* **58,** 761–767 (2002).
67. Chapman, M. S. Restrained real-space macromolecular atomic refinement using a new resolution-dependent electron-density function. *Acta Crystallogr. A* **51,** 69–80 (1995).
68. Gonen, T. *et al.* Lipid-protein interactions in double-layered two-dimensional AQP0 crystals. *Nature* **438,** 633–638 (2005).
69. Zhou, G., Wang, J., Blanc, E. & Chapman, M. S. Determination of the relative precision of atoms in a macromolecular structure. *Acta Crystallogr. D* **54,** 391–399 (1998).
70. Laurberg, M. *et al.* Structural basis for translation termination on the 70S ribosome. *Nature* **454,** 852–857 (2008).
71. Adams, P. D. *et al.* The Phenix software for automated determination of macromolecular structures. *Methods* **55,** 94–106 (2011).
72. Brunger, A. T. Version 1.2 of the crystallography and NMR system. *Nat. Protocols* **2,** 2728–2733 (2007).
73. Chen, V. B. *et al.* MolProbity: all-atom structure validation for macromolecular crystallography. *Acta Crystallogr. D* **66,** 12–21 (2010).
74. DeLano, W. L. *The PyMOL Molecular Graphics System* (DeLano Scientific, 2002).
75. Tinoco, I. Jr & Gonzalez, R. L. Jr. Biological mechanisms, one molecule at a time. *Genes Dev.* **25,** 1205–1231 (2011).
76. Gonzalez, R. L. Jr, Chu, S. & Puglisi, J. D. Thiostrepton inhibition of tRNA delivery to the ribosome. *RNA* **13,** 2091–2097 (2007).
77. Engh, R. A. & Huber, R. Accurate bond and angle parameters for X-ray protein structure refinement. *Acta Cryst* **A 47,** 392–400 (1991).

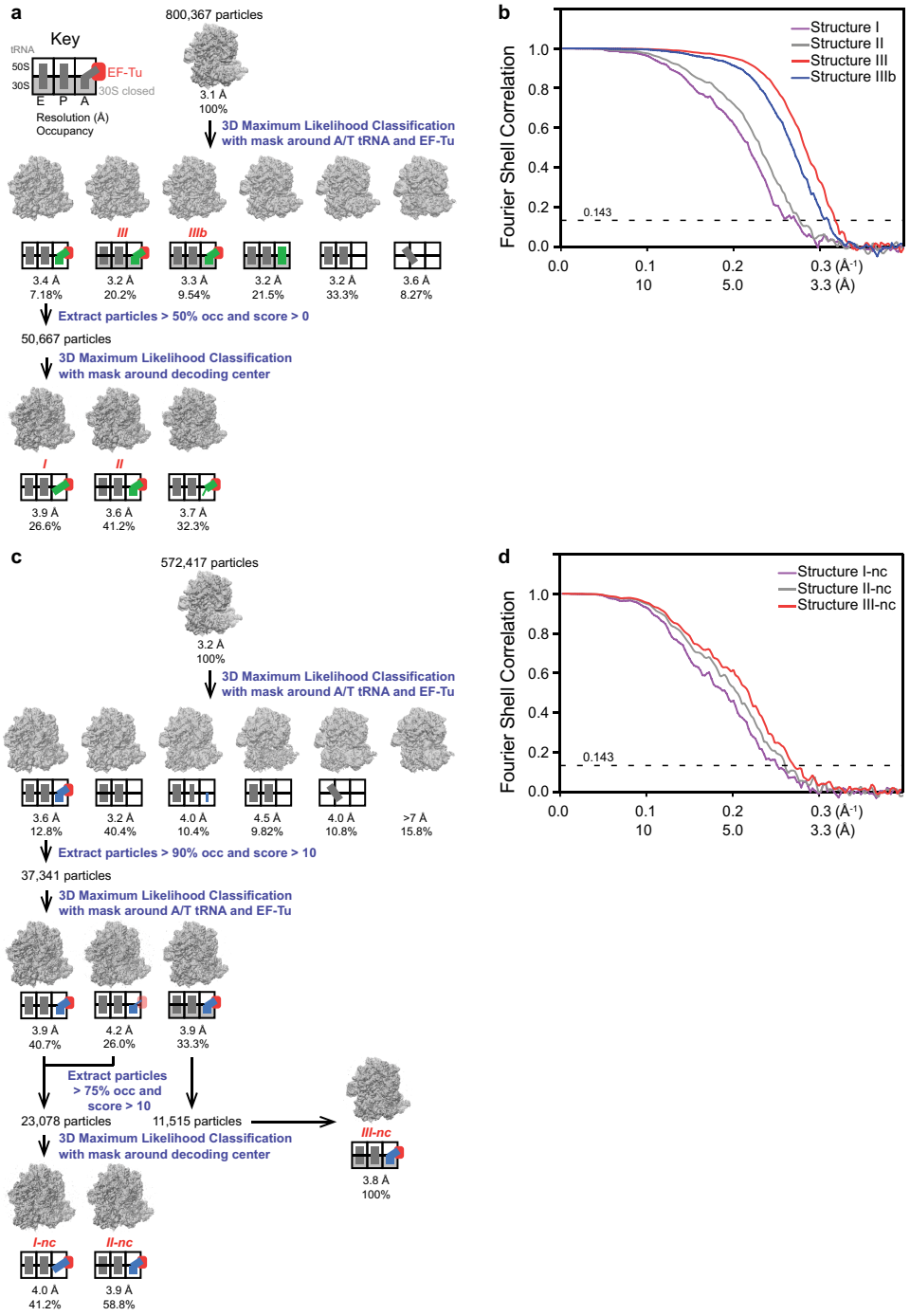

Extended Data Figure 1 | Overview of classification procedures and resolution curves for all structures. a, Scheme of refinement and classification procedures for the cognate dataset. **b**, Fourier shell correlation (FSC) curves for the cognate structures. **c**, Scheme of refinement and classification procedures for the near-cognate dataset. **d**, FSC curves for the near-cognate structures.

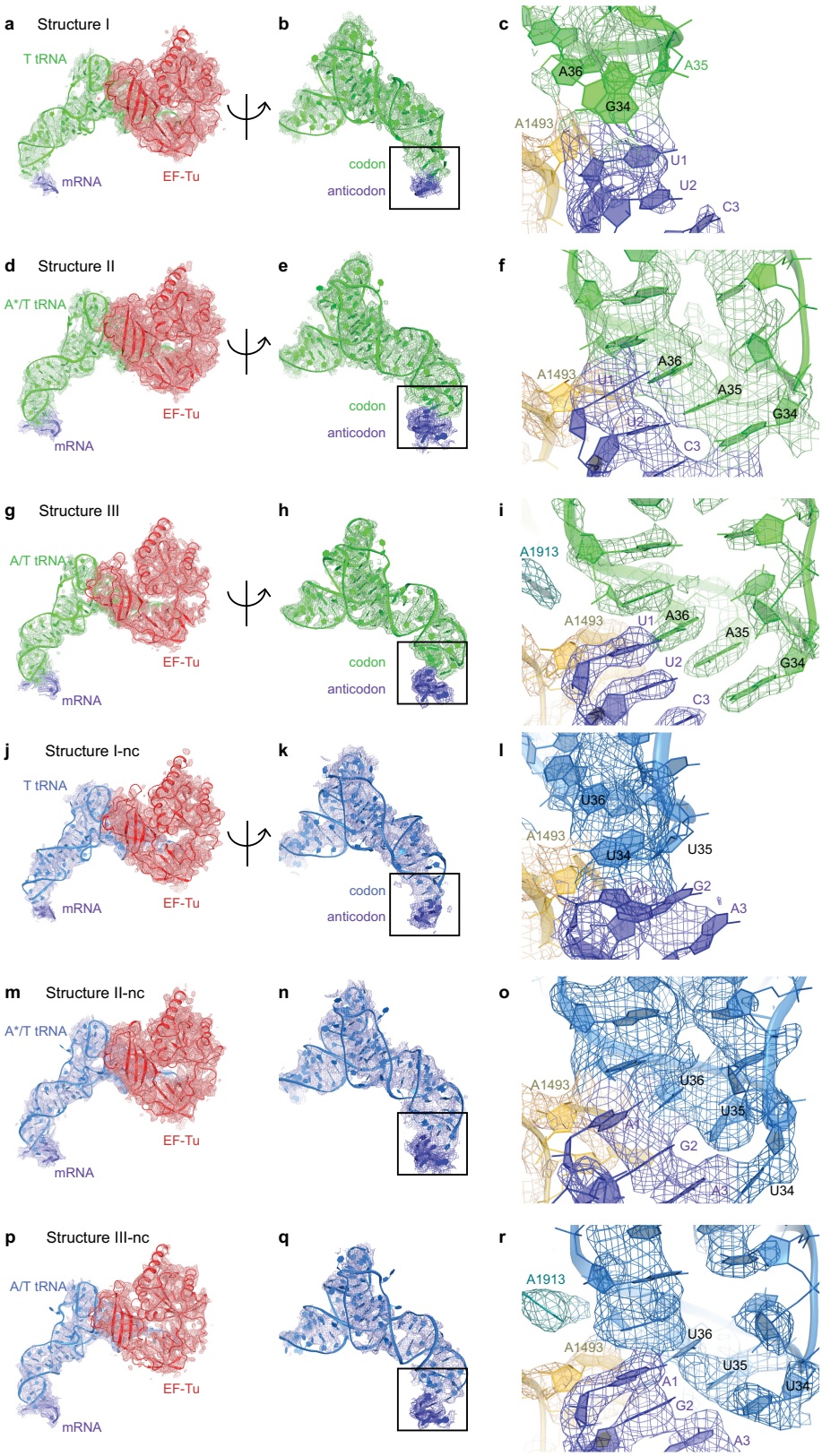

Extended Data Figure 2 | See next page for caption.

Extended Data Figure 2 | Cryo-EM densities for ternary complex in each structure. a, Cryo-EM density for ternary complex and codon in structure I is shown at 3σ after applying a B-factor of −36 Å^2. **b**, Cryo-EM density for cognate tRNA and codon in structure I is shown as in **a**. **c**, Cryo-EM density for the anticodon and codon, which are not base paired, in structure I is shown at 4σ after applying a B-factor of −36 Å^2. **d**, Cryo-EM density for ternary complex and codon in structure II is shown at 3σ after applying a B-factor of −50 Å^2. **e**, Cryo-EM density for cognate tRNA and codon in structure II is shown as in **d**. **f**, Cryo-EM density for the anticodon and codon, which are base paired, in structure II is shown at 4.5σ after applying a B-factor of −50 Å^2. **g**, Cryo-EM density for ternary complex and codon in structure III is shown at 4σ after applying a B-factor of −100 Å^2. **h**, Cryo-EM density for cognate tRNA and codon in structure II is shown as in **g**. **i**, Cryo-EM density for the anticodon and codon, which are base paired, in structure III is shown at 5σ after applying a B-factor of −150 Å^2. **j**, Cryo-EM density for ternary complex and codon in structure I-nc is shown at 3σ. **k**, Cryo-EM density for near-cognate tRNA and codon in structure I-nc is shown as in **j**. **l**, Cryo-EM density for the anticodon and codon, which are not base paired, in structure I-nc is shown at 3.5σ for T tRNA and 16S rRNA or 4σ for mRNA. **m**, Cryo-EM density for ternary complex and codon in structure II-nc is shown at 3σ after applying a B-factor of −25 Å^2. **n**, Cryo-EM density for near-cognate A*/T tRNA and codon in structure II-nc is shown as in **m**. **o**, Cryo-EM density for the anticodon and codon, which are interacting in structure II-nc is shown at 4.5σ after applying a B-factor of −25 Å^2. **p**, Cryo-EM density for ternary complex and codon in structure III-nc is shown at 4σ after applying a B-factor of −50 Å^2. **q**, Cryo-EM density for near-cognate tRNA and codon in structure II-nc is shown as in **p**. **r**, Cryo-EM density for the anticodon and codon, which are base paired, in structure III-nc is shown at 5.2σ after applying a B-factor of −60 Å^2.

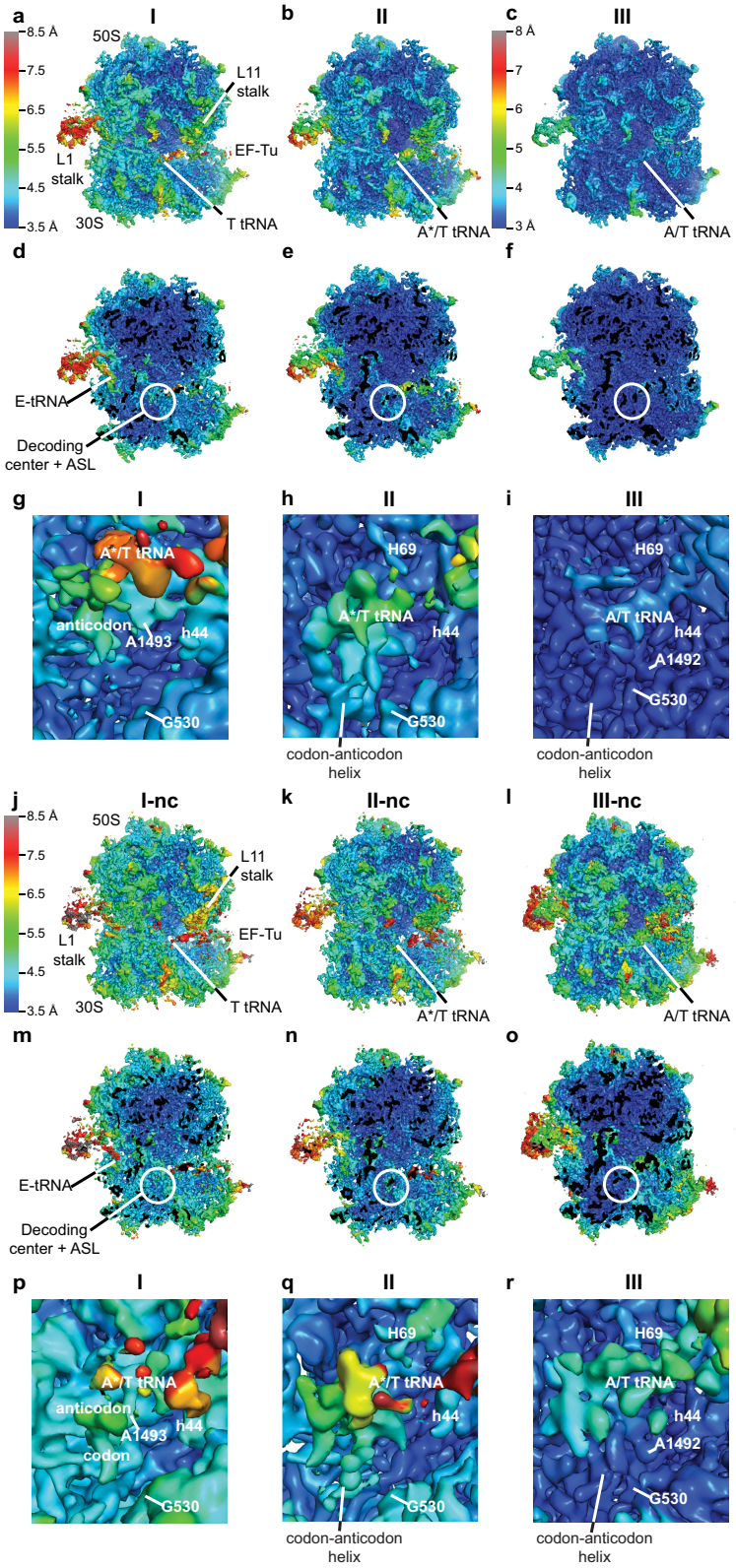

Extended Data Figure 3 | See next page for caption.

Extended Data Figure 3 | Local resolution of cryo-EM maps of the cognate and near-cognate complexes. Local resolution of each cryo-EM map was determined using Blocres. **a**, An overview of the structure I map. The unsharpened map is shown at 5σ, coloured using a scale ranging from 3.5 Å to 8.5 Å (left). **b**, An overview of the structure II map shown as in **a**. **c**, An overview of the structure III map. The unsharpened map is shown at 5σ, coloured using a scale ranging from 3.0 Å to 8.0 Å (left). **d**–**f**, Slab views at the ribosome interior in maps corresponding to structure I (**d**), structure II (**e**) and structure III (**f**), prepared and coloured as in **a**, **b** and **c**, respectively. **g**, Close-up view of decoding centre of structure I. The map was sharpened by applying a B-factor of −36 Å^2 and is shown at 4.5σ, coloured as in **a**. **h**, Close-up view of decoding centre of structure II. The map was sharpened by applying a B-factor of −50 Å^2 and is shown at 5σ, coloured as in **a**. **i**, Close-up view of decoding centre of structure III. The map was sharpened by applying a B-factor of −100 Å^2 and is shown at 4σ, coloured as in **c**. **j**, An overview of the structure I-nc map. The unsharpened map is shown at 5σ and is coloured using a scale ranging from 3.5 Å to 8.5 Å (left). **k**, An overview of the structure II-nc map, as in **j**. **l**, An overview of the structure III-nc map, as in **j**. **m**–**o**, Slab views at the ribosome interior in maps corresponding to structure I-nc (**m**), structure II-nc (**n**) and structure III-nc (**o**), prepared and coloured as in **j**. **p**, Close-up view of decoding centre of structure I-nc. The unsharpened map is shown at 4.5σ, coloured as in **j**. **q**, Close-up view of decoding centre of structure II-nc. The map was sharpened by applying a B-factor of −25 Å^2 and is shown at 5σ, coloured as in **j**. **r**, Close-up view of the decoding centre of structure III-nc. The map was sharpened by applying a B-factor of −50 Å^2 and is shown at 5σ, coloured as in **j**.

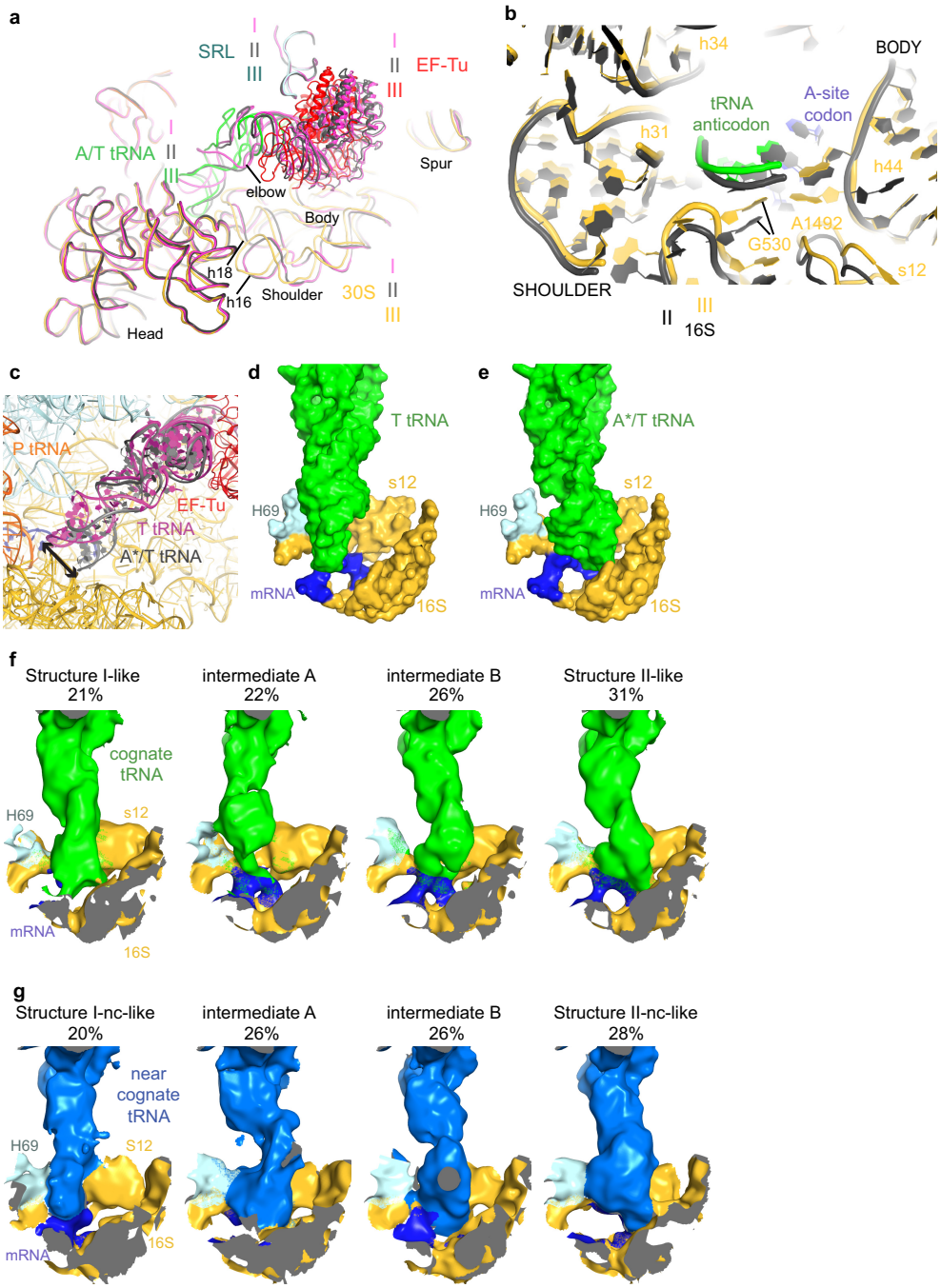

Extended Data Figure 4 | 30S domain closure and aminoacyl-tRNA conformations in cognate and near-cognate complexes. a, Comparison of the 30S conformations among structures I (magenta), II (grey) and III (multi-coloured). Superposition was achieved by structural alignment of 23S rRNA. **b**, Superposition of structure II (grey) and III (multi-coloured) highlighting the movement of the shoulder including the 530 loop towards the 30S body including h44. **c**, Different conformations of aminoacyl-tRNA in structures I and II: T tRNA (structure I) is relaxed, whereas A*/T tRNA (structure II) is kinked to base-pair with mRNA. **d**, Interaction of T tRNA in structure I with the decoding centre is shown in surface representation. All atoms within 15 Å of residues 30–38 of T tRNA are shown except for 16S residues 950–964 and 984–985, which were omitted for clarity. **e**, Interaction of A*/T tRNA in structure II with the decoding centre is shown in surface representation as in **d**. **f**, Cognate tRNA anticodon samples positions between those in structures I and II. Additional focused classification into four classes revealed intermediate classes with A-site tRNA density midway between the T tRNA and A*/T tRNA conformations. The cryo-EM density, within 15 Å of residues 30–38 of T or A*/T tRNA, is shown with exceptions as in **d**, at 3σ after applying a B-factor of +200 Å^2. **g**, Near-cognate tRNA anticodon samples positions between those in structure I-nc and structure II-nc. Additional focused classification into four classes revealed intermediate classes with A-site tRNA density midway between the T tRNA and A*/T tRNA conformations. The cryo-EM density is shown as in **f**.

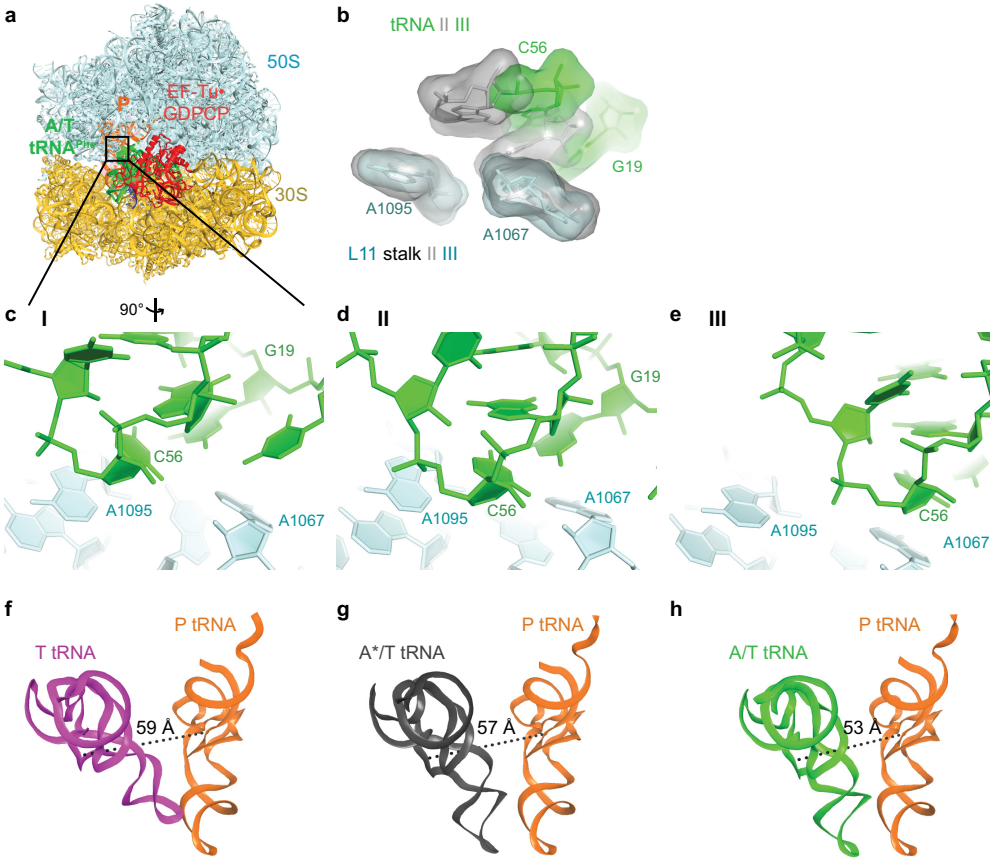

Extended Data Figure 5 | Sliding of tRNA elbow along the L11 stalk from structures I–III towards the P-site tRNA agrees with distance changes inferred from smFRET studies of tRNA decoding. a, Overview of structure III with box highlighting the location of tRNA elbow and L11 stalk. **b**, tRNA elbow residues G19 and C57 slide along L11 stalk residues 1095 and 1067 from structure II (grey) to structure III (green). Superposition was achieved by aligning on residues 1095 and 1067 of L11 stalk. **c**, The elbow of T tRNA (green) and L11 stalk in structure I. **d**, The elbow of A*/T tRNA (green) and L11 stalk in structure II. **e**, The elbow of A/T tRNA (green) and L11 stalk in structure III. **f**, The distance between nucleotide 47 of T tRNA (magenta) and nucleotide 8 of P-site tRNA (orange) is shown. These locations were used in smFRET studies of tRNA decoding[8,76]. **g**, The distance between nucleotide 47 of A*/T tRNA (grey) and nucleotide 8 of P-site tRNA (orange) is shown. **h**, The distance between nucleotide 47 of A/T tRNA (green) and nucleotide 8 of P-site tRNA (orange) is shown. The distance changes between T or A*/T tRNA to A/T tRNA are consistent with the change from a low FRET value of 0.35 in the early tRNA decoding states to a mid-FRET value of 0.5 in the GTP activated tRNA decoding state, as described in the Methods.

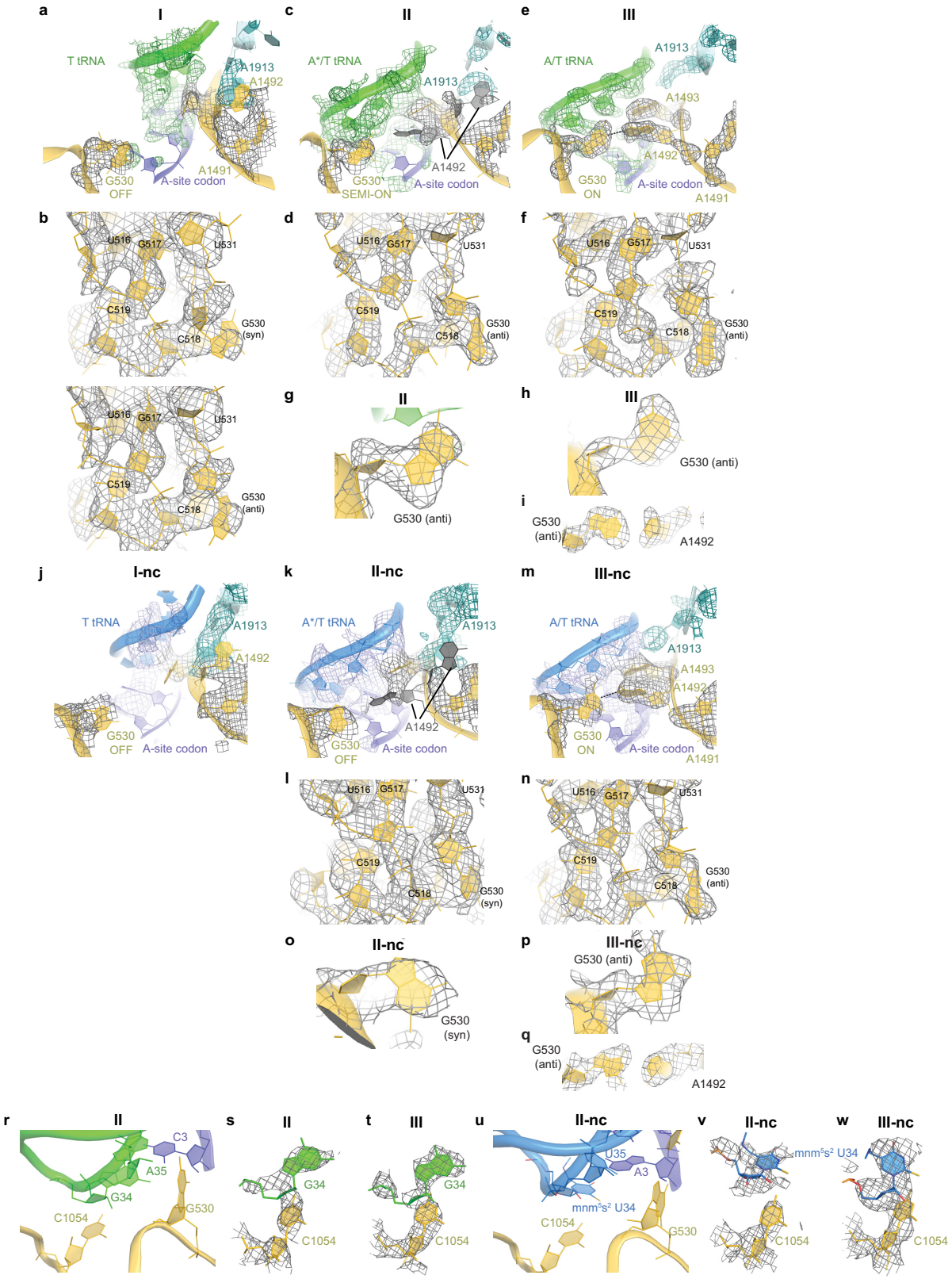

Extended Data Figure 6 | See next page for caption.

Extended Data Figure 6 | Conformational differences in the decoding centres of cognate and near-cognate structures I–III. a, Cryo-EM density (shown as mesh) of the decoding centre in structure I. The map was sharpened by applying a B-factor of −36 Å^2 and density is shown at 3.5σ for mRNA and anticodon of T tRNA, 5.5σ for G530, 4.0σ for A1492, A1493 and A1913. **b**, Cryo-EM density for the G530 region in structure I is shown with two conformations of G530-syn (top) and G530-anti (bottom). Both conformations fit with similar local cross-correlation coefficients (Methods). The map was sharpened by applying a B-factor of −75 Å^2 and density is shown at 5σ. **c**, Cryo-EM density for the decoding centre in structure II. The map was sharpened by applying a B-factor of −75 Å^2 and density is shown at 5.5σ for G530 or at 4σ for the mRNA and the anticodon of A*/T tRNA, A1492, A1493 and A1913. Density for residue 1492 (shown in grey) is compatible with two conformations, in and out of h44. **d**, Cryo-EM density for the G530 region in structure II. The map was sharpened by applying a B-factor of −100 Å^2 and density is shown at 5σ. **e**, Cryo-EM density for the decoding centre in structure III. The map was sharpened by applying a B-factor of −150 Å^2 and density is shown at 4.5σ for the mRNA and the anticodon of A/T tRNA, G530, A1492, A1493 and A1913. **f**, Cryo-EM density for the G530 region in structure III. The map was sharpened by applying a B-factor of −150 Å^2 and density is shown at 5σ. **g**, Cryo-EM density (grey mesh) showing the anti-conformation of G530 (yellow model) in structure II. The map was sharpened by applying a B-factor of −100 Å^2 and density is shown at 5σ. **h**, **i**, Cryo-EM density showing the anti-conformation of G530 in structure III. The map was sharpened by applying a B-factor of −150 Å^2 and density is shown at 5σ. **j**, Cryo-EM density of the decoding centre in structure I-nc. The map was not B-factor sharpened and density is shown at 3.75σ for mRNA, the anticodon of T tRNA, A1492, A1493 and A1913, or at 5σ for G530. **k**, Cryo-EM density for the decoding centre in structure II-nc. The map was sharpened by applying a B-factor of −25 Å^2 and density is shown at 4.3σ for mRNA, the anticodon of tRNA, A1492, A1493 and A1913, or at 5.5σ for G530. **l**, Cryo-EM density of structure II-nc for the 30S shoulder including G530. The map was sharpened by applying a B-factor of −120 Å^2 and density is shown at 3.5σ. **m**, Cryo-EM density for the decoding centre in structure III-nc. The map was sharpened by applying a B-factor of −50 Å^2 and density is shown at 4.75σ for mRNA and the anticodon of tRNA, G530, A1492 and A1493, and at 4.5 for A1913. **n**, Cryo-EM density of structure III-nc for the 30S shoulder including G530. The map was sharpened by applying a B-factor of −100 Å^2 and density is shown at 4.5σ. **o**, Cryo-EM density showing the syn-conformation of G530 in structure II-nc. The map was sharpened by applying a B-factor of −120 Å^2 and density is shown at 3.7σ. **p**, **q**, Cryo-EM density showing the anti-conformation of G530 in structure III-nc. The map was sharpened by applying a B-factor of −120 Å^2 and density is shown at 3.3σ. **r**, Nucleotide 34 of the anticodon stacks on C1054 in the cognate structure II. **s**, Cryo-EM density (grey mesh) for the cognate structure II. The map was sharpened by applying a B-factor of −100 Å^2 and density is shown at 5σ. **t**, Cryo-EM density for the cognate structure III. The map was sharpened by applying a B-factor of −150 Å^2 and density is shown at 5.5σ. **u**, Nucleotide 34 of the near-cognate anticodon in structure II-nc is shifted by approximately 2 Å from C1054, relative to its position in the cognate complex (shown in **r**). **v**, Cryo-EM density for the near-cognate structure II-nc. The map was sharpened by applying a B-factor of −120 Å^2 and density is shown at 3.5σ. **w**, Cryo-EM density for the near-cognate structure III-nc. The map was sharpened by applying a B-factor of −50 Å^2 and density is shown at 5.5σ. Modification of U34 of tRNA^{Lys} to 5-methylaminomethyl-2-thiouridine (mnm^{5}s^{2}U34) is shown in **u**–**w**.

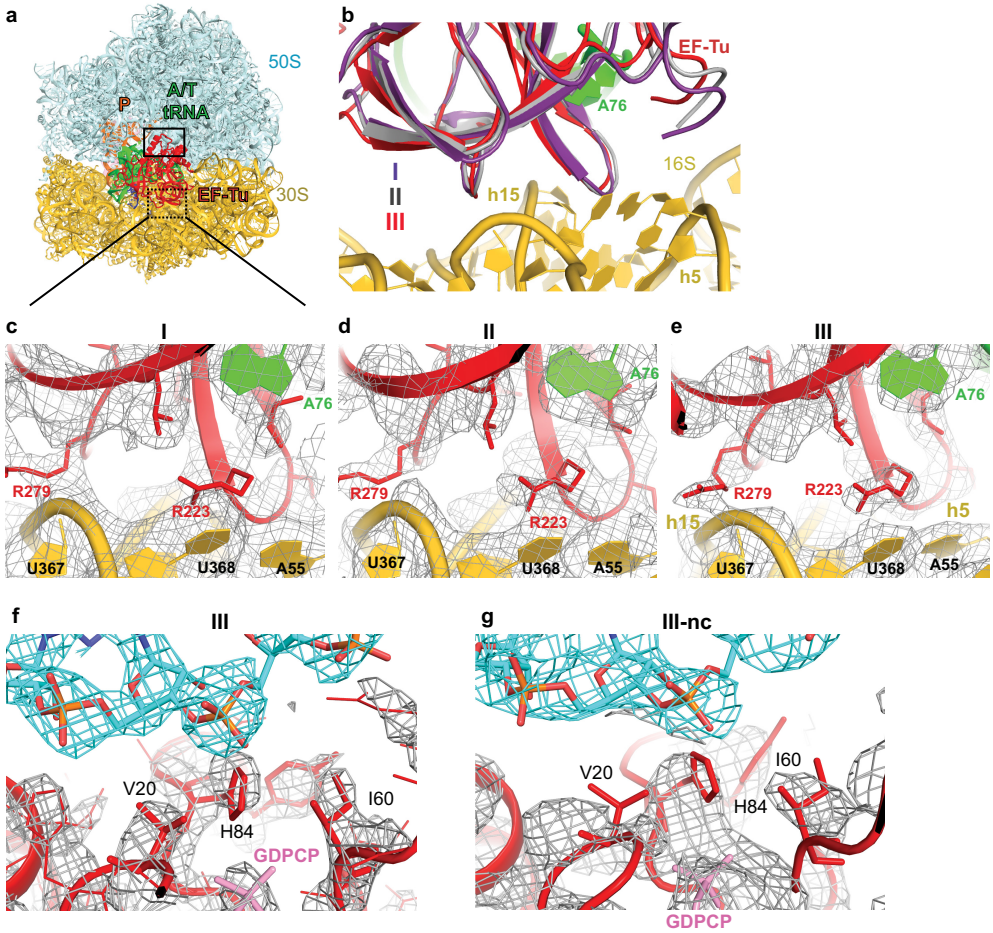

Extended Data Figure 7 | Anchoring of EF-Tu to the 30S shoulder in structures I, II and III and to the SRL in structures III and III-nc. **a**, Overview of structure III with boxes highlighting locations of EF-Tu contacts to 30S shoulder (dashed box) and to SRL (solid box). **b**, The contacts of EF-Tu with the 30S shoulder are similar among structures I (purple), II (grey) and III (red). **c**, Cryo-EM density for EF-Tu (red) and 16S rRNA (pale yellow) in structure I. The map was sharpened by applying a B-factor of −36 Å^2 and is shown at 3σ. **d**, Cryo-EM density for EF-Tu and 16S rRNA in structure II. The map was sharpened by applying a B-factor of −75 Å^2 and is shown at 3.5σ. **e**, Cryo-EM density for EF-Tu and 16S rRNA in structure III. The map was sharpened by applying a B-factor of −100 Å^2 and is shown at 4.5σ. **f**, Cryo-EM density for EF-Tu (red) and the SRL of 23S rRNA (pale cyan) in structure III. The map was sharpened by applying a B-factor of −150 Å^2 and is shown at 4.5σ. **g**, Cryo-EM density for EF-Tu and SRL of 23S rRNA in structure III-nc. The map was sharpened by applying a B-factor of −50 Å^2 and is shown at 4.5σ.

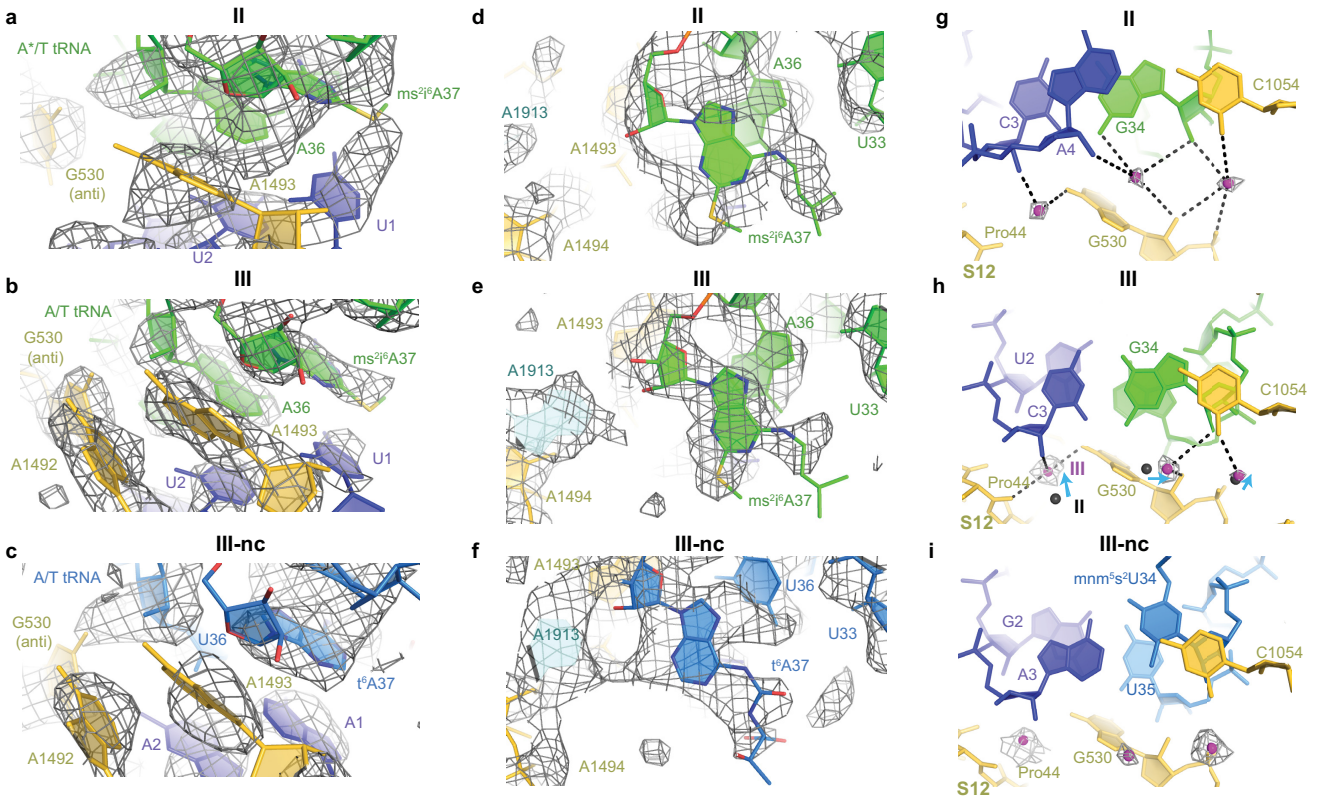

Extended Data Figure 8 | Modifications of A37 in tRNA^{Phe} and tRNA^{Lys}, and magnesium ion coordination near G530. a, Cryo-EM density for the codon–anticodon helix in structure II shows that the 2-methylthio moiety of 2-methylthio-N^6-(2-isopentenyl)-adenosine at position 37 of tRNA^{Phe} (ms^2i^6A37) stacks on U1 of the A-site codon. The map was sharpened by applying a B-factor of −75 Å^2 and density is shown at 4.8σ. **b**, Cryo-EM density for the codon–anticodon helix in structure III shows that ms^2i^6A37 of tRNA^{Phe} stacks on U1 similarly to that in structure II. The map was sharpened by applying a B-factor of −150 Å^2 and density is shown at 6σ. **c**, Cryo-EM density for the codon–anticodon helix in structure III-nc shows that 6-threonylcarbamoyl adenosine at position 37 of tRNA^{Lys} (t^6A37) stacks on A1. The map was sharpened by applying a B-factor of −120 Å^2 and density is shown at 4.5σ. **d**, Cryo-EM density for structure II shows the N^6 modification of ms^2i^6A37 of tRNA^{Phe} in close proximity to U33. The map was sharpened by applying a B-factor of −75 Å^2 and density is shown at 4σ. **e**, Cryo-EM density for structure III shows the N^6 modification of ms^2i^6A37 of tRNA^{Phe} in close proximity to U33. The map was sharpened by applying a B-factor of −150 Å^2 and density is shown at 4σ. **f**, Cryo-EM density for structure III-nc shows the N^6 modification of t^6A37 of tRNA^{Lys}. The map was sharpened by applying a B-factor of −120 Å^2 and density is shown at 3.5σ. **g**, In structure II, three magnesium ions (magenta) are coordinated (dotted lines) by G530 and codon–anticodon helix (in some instances, the coordination probably occurs via water molecules). Density for magnesium ions (mesh) was sharpened by applying a B-factor of −75 Å^2, shown at 4σ. **h**, In structure III, the magnesium ions shift with G530. Density was sharpened by applying a B-factor of −150 Å^2, shown at 4σ. **i**, In structure III-nc, three magnesium ions are seen at equivalent position to those in structure III. Density was sharpened by applying a B-factor of −120 Å^2, shown at 3σ.

Extended Data Table 1 | Refinement statistics for all structures

	Structure I	Structure II	Structure III	Structure I-nc	Structure II-nc	Structure III-nc
PDB code	5UYK	5UYL	5UYM	5UYN	5UYP	5UYQ
EMDB code	8615	8616	8617	8618	8619	8620
Data collection						
EM equipment	FEI Titan Krios	FEI Titan Krios	FEI Titan Krios	FEI Titan Krios	FEI Titan Krios	FEI Titan Krios
Voltage (kV)	300	300	300	300	300	300
Detector	K2 summit	K2 summit	K2 summit	K2 summit	K2 summit	K2 summit
Pixel size (Å)	1.64	1.64	1.64	1.64	1.64	1.64
Electron dose ($e^-/Å^2$)	50	50	50	30	30	30
Defocus range (μm)	0.4 – 5.0	0.4 – 5.0	0.4 – 5.0	0.5 – 5.0	0.5 – 5.0	0.5 – 5.0
Reconstruction						
Software	Frealign v9.10-9.11	Frealign v9.10-9.11	Frealign v9.10-9.11	Frealign v9.10-9.11	Frealign v9.10-9.11	Frealign v9.10-9.11
Number of particles in final map	6,726	10,431	153,597	4,629	6,910	5,758
Final resolution (Å)	3.9	3.6	3.2	4	3.9	3.8
Map-sharpening *B* factor ($Å^2$)	-36	-50	-100	0	-25	-25
Model fitting						
Software	Chimera & Pymol	Chimera & Pymol	Chimera & Pymol	Chimera & Pymol	Chimera & Pymol	Chimera & Pymol
Model composition						
Non-hydrogen atoms	154,413	153,755	154,140	153,718	153,781	153,760
Protein residues	6,563	6,476	6,476	6,474	6,476	6,476
RNA bases	4,812	4,810	4,810	4,809	4,811	4,810
Ligands (Zn^{2+}/Mg^{2+})	0, 0	0, 0	2, 383	0, 0	0, 0	0, 1
Ligands/Modifications (GDPCP, fMet, Phe, Lys)	1 (GDPCP)	3 (GDPCP, fMet, Phe)	3 (GDPCP, fMet, Phe)	1 (GDPCP)	3 (GDPCP, fMet, Lys)	3 (GDPCP, fMet, Lys)
Refinement						
Software	RSRef & Phenix	RSRef & Phenix	RSRef & Phenix	RSRef & Phenix	RSRef & Phenix	RSRef & Phenix
Correlation Coefficient *	0.84	0.84	0.88	0.79	0.80	0.79
Real space R-factor †	0.19	0.19	0.20	0.20	0.20	0.20
Validation (proteins)						
Molprobity Score ‡	2.22	2.31	2.31	2.4	2.5	2.4
Clash score, all atoms ‡	12.0	13.1	13.0	13.6	13.3	14.5
Poor rotamers (%) ‡	0.9	1.1	1.2	1.1	1.6	1.3
Favored rotamers (%) ‡	94.9	93.8	94.6	93.6	92.8	92.9
Ramachandran-plot statistics						
Outlier (%) ‡	1.7	2.2	2.0	2.8	3.1	2.7
Favored (%) ‡	86.4	85.6	86.5	83.5	82.6	84.5
R.m.s. deviations †,§						
Bond length (Å)	0.007	0.008	0.006	0.005	0.005	0.005
Bond angle (°)	0.9	0.9	0.9	0.9	0.9	0.9
Validation (RNA)						
Good sugar puckers (%) ‡	99.6	99.5	99.5	99.6	99.6	99.4
Good backbone conformation (%) ‡	88.4	88.2	88.4	88.4	88.3	87.1

*All-atom correlation coefficient as reported by phenix.real_space_refine[71].
†As reported by RSRef[67].
‡As reported by Molprobity[73].
§Root mean square deviation (r.m.s.d.) values from ideal covalent bond lengths and angles[77].

Extended Data Table 2 | Distances among cognate structures I to III and near-cognate structures I-nc to III-nc, reflecting movements of the 30S shoulder domain relative to the head and body of the 30S subunit

Region	Distance* (RMSD, all-atom), Å			Distance* (RMSD, all-atom), Å			Distance* (RMSD, all-atom), Å		
	I to II	I to III	II to III	I-nc to II-nc	II-nc to III-nc	I-nc to III-nc	I to I-nc	II to II-nc	III to III-nc
50S subunit, used to align 70S ribosomes (23S rRNA, excluding L1 and L11 stalks)	0.46	0.51	0.47	0.52	0.71	0.71	0.57	0.56	0.66
Body, 30S central region (nt 580-920 of 16S rRNA)	0.49	1.4	1.4	0.52	1.1	1.1	0.61	0.58	0.75
Head (nt 960-1400 of 16S rRNA)	0.56	1.6	1.7	0.60	1.2	1.2	0.71	0.75	0.86
Shoulder, near 30S center (h18, nt 510-540, 16S rRNA)	0.90	**3.2**	**3.2**	0.78	**2.8**	**2.7**	0.89	0.93	0.85
Shoulder, periphery (h16, nt 400-440)	0.54	**4.6**	**4.6**	0.58	**4.3**	**4.1**	0.65	0.67	0.88

*R.m.s.d. values that are more than 3× r.m.s.d. values for the 23S rRNA, are shown in bold blue font. Superposition of structures relative to each other was obtained by structural alignment of 23S rRNA excluding the L1 and L11 stalks.

doi:10.1038/nature22397

Choice of ternary complex tRNA: tRNA^{Phe} and tRNA^{Lys}

We chose to study EF-Tu-ternary-complex pre-accommodation using tRNA^{Phe}, because tRNA^{Phe} is commonly used in studies of tRNA decoding [32,33,35], and we recently identified intermediate states of tRNA^{Phe} binding in the presence of RelA [29]. To visualize a near-cognate ternary complex with detectable binding to the ribosome, we considered introducing a G-U mismatch in the codon-anticodon interaction. This, however, is impossible for tRNA^{Phe}, which contains adenosines in the first two positions of the anticodon. We chose tRNA^{Lys}, a well-studied tRNA that allows formation of a G-U mismatch. The binding affinities and rate of GTP hydrolysis by ternary complexes bearing tRNA^{Lys} and tRNA^{Phe} during decoding are nearly identical [36,37], and both tRNAs have similar accuracies of initial selection in vitro [38]. These considerations justify the comparison of the two cryo-EM complexes.

Intermediate conformations of tRNA between T and A*/T tRNA in the cognate and near-cognate complexes

Having identified relaxed (T state, Structures I and I-nc) and kinked (A*/T state, Structures II and II-nc) aa-tRNA conformations on the 30S-domain-open ribosome, we sought further insight into the dynamics of the aa-tRNAs in the DC. We performed an A-site-focused sub-classification of cryo-EM data obtained for the cognate tRNA^{Phe} and near-cognate tRNA^{Lys} complexes (see **Methods**). For both complexes, we identified additional classes of maps with density between the relaxed and kinked conformations of ASLs (**Extended Data Fig. 4f-g**), but low resolution precluded detailed modeling of these conformations. Thus, our data indicate that cognate and near-cognate tRNAs sample multiple conformations in the A site of the open 30S subunit, ranging from the T-tRNA to the A*/T-tRNA state.

Interactions of ternary complexes with the L11 stalk

From Structure I to Structure III, the tRNA binds deeper into the 30S A site. The acceptor arm shifts as much as 7 Å toward the peptidyl-tRNA (P-tRNA) as the elbow

slides along the L11 stalk (**Extended Data Fig. 5**). In Structure I, where the T-tRNA elbow is furthest removed from the P-tRNA elbow, nucleotide A1067 of the L11 stalk (helix 43 of the 23S rRNA) interacts with G19 of the T tRNA, while A1095 of the L11 stalk interacts with C57 (**Extended Data Fig. 5c**). In Structure II, A1067 interacts with both G19 and C57 of the A*/T tRNA (**Extended Data Fig. 5d**). Finally, in Structure III, A1067 stacks onto C57 of the A/T tRNA (**Extended Data Fig. 5e**). Data classification revealed an additional 30S-domain-closed state (IIIb), which differed from Structure III in that the L11 stalk is poorly ordered. Together, the structures show that the L11 stalk dynamically interacts with the tRNA elbow and contributes to tRNA pre-accommodation.

From Structure I-nc to III-nc, the tRNA elbow moves past A1067 of the L11 stalk in a manner analogous to that in the cognate complex. These observations agree with the finding that mutation of A1067 equally impairs the ability of cognate and near-cognate ternary complexes to bind the ribosome and hydrolyze GTP [78].

Roles of tRNA modifications in stabilizing the codon-anticodon helix

Post-transcriptional modification of the anticodon (nucleotides 34-36) and the adjacent nucleotide 37 of tRNA modulate tRNA structure and interactions with the ribosome (reviewed in ref [79,80]). Hyper-modifications of purine 37 have been found in tRNAs that contain uridine or adenosine in at least two positions of the anticodon. This suggests that modification of nucleotide 37 is involved in stabilizing the codon-anticodon helix. Indeed, the 2-methylthio moiety of 2-methylthio-N6-(2-isopentenyl)-adenosine from $tRNA^{Phe}$ stacks on the U1 base of the codon in Structures II and III (**Extended Data Fig. 8a-b**), consistent with stabilization of the base-paired codon-anticodon helix. The ~5-Å-long extensions from the N6 atom of A37 in both $tRNA^{Phe}$ (Structures II and III) and $tRNA^{Lys}$ (Structure III-nc) are resolved and approach the ribose of U33 (**Extended Data Fig. 8d-f**), consistent with the role of the modifications in stabilization of the U-turn of the ASL [81,82]. Nucleotide 37 lies >10 Å from G530 (**Extended Data Fig. 8a-c**), so hyper-modification of A37 is unlikely to directly affect the G530 latch during decoding. The wobble nucleotide 34, however, is closer to G530. Though G530 does not contact 5-methylaminomethyl-2-thiouridine 34 in $tRNA^{Lys}$ (the S2 atom is closest to G530 in Structure III-nc: ~6-Å away; **Extended Data Fig. 6u-w**), modifications in other tRNAs might interact with G530 and modulate the G530 latch.

Interactions of G530 with magnesium ions

The accuracy of tRNA decoding is sensitive to magnesium-ion concentration [5,12,38,83]. Aided by the backbone of the codon-anticodon helix and 16S rRNA, G530 coordinates at least three magnesium ions in both the SEMI-ON (Structure II) and ON (Structure III) conformations. The magnesium ions shift with G530 as G530 latches the DC (**Extended Data Fig. 8g-h**). In the near-cognate Structure III-nc, density shows magnesium ions next to G530 positioned similarly to those in the cognate Structure III (**Extended Data Fig. 8h-i**). Stabilization of G530 in the SEMI-ON and ON conformations by magnesium is consistent with the observation that increasing the magnesium concentration reduces accuracy of initial selection [5,12,38,83].

E-site tRNA

Density for the E-site tRNA is present in all six maps, but its lower resolution did not allow unambiguous determination of tRNA identity. We therefore modeled E-tRNA as $tRNA^{fMet}$ (see **Methods**). Additional sub-classification of the E site in the cognate complex revealed tRNA positions that differ by as much as 6 Å. We did not observe a correlation between E-tRNA position and A site conformation. A correlation is predicted by the allosteric three-site model, which postulates that aa-tRNA binding involves negative cooperativity between the A and E sites [84]. We note, however, that a study of complexes with deacyl-tRNA cognate to the E-site codon is necessary to directly address this hypothesis.

Structures of early intermediates of cognate and near-cognate complexes are consistent with biochemical and biophysical data

Structures I and II are in excellent agreement with structural information available from single-molecule Förster resonance energy transfer (smFRET) studies. Monitoring of the step-wise binding of cognate EF-Tu ternary complexes to the ribosome [8,76,85] revealed an early, short-lived “low-FRET” step that was followed by a “mid-FRET” state. We estimate (see **Methods**) that the shift between the low-FRET and mid-FRET states corresponds to a 4- to 6-Å movement of the accommodating aa-tRNA toward the P-site

tRNA [8,76,85] (see **Methods**). This agrees with our observation that the corresponding nucleotides in Structures I and II are 4 to 6 Å farther apart than in Structure III (**Extended Data Fig. 5f-h**), indicating that T tRNA and A*/T tRNA in Structures I and II are equivalent to the early, low-FRET, pre-accommodation intermediates.

Our observations of near-cognate Structures I-nc, II-nc and III-nc and their distribution are consistent with biochemical, structural, and biophysical data. Fluorescent quenching experiments showed that near-cognate and cognate aminoacyl-tRNAs adopt similar conformations as the ternary complexes bind the ribosome [86], consistent with our observations. A 13.2-Å resolution cryo-EM structure with near-cognate EF-Tu ternary complex in a post-GTP hydrolysis state stabilized on ribosomes by kirromycin [87] showed A/T-like tRNA bound to the closed 30S subunit and EF-Tu docked at the SRL, consistent with GTPase-activated Structure III-nc. Moreover, smFRET studies suggest that both early and late pre-accommodation intermediates are globally similar between cognate and near-cognate aa-tRNAs [8]. In general agreement with our estimation of particle distribution, early smFRET intermediates are preferred over late intermediates for near-cognate ternary complexes and the late intermediates dominate for cognate ternary complexes, in the presence of either GTP or non-hydrolyzable GDPNP [8]. Direct quantitative comparisons between our structural results and various biophysical or biochemical data are difficult to perform because of differences in tRNA identities and buffer conditions, to which the accommodation assays are highly sensitive [5,7,12,38,83].

G530 mutational studies support critical structural role

The critical structural role of G530 is emphasized by mutational studies, which showed that G530 is indispensable for EF-Tu-dependent aa-tRNA binding [39], EF-Tu GTPase activation [40] and translation efficiency [41-43]. A G530A mutation reduces the rate of GTP hydrolysis ~20-fold [40], suggesting that G530A alters the hydrogen bonding network, thereby impairing the G530 latch. Similarly, modifications of 2'-hydroxyls of the anticodon nucleotides 35-36, which base pair with the 2nd and 1st codon nucleotides and interact with G530, reduce tRNA binding affinity in the A site (2'–deoxy; [88]) and codon-reading efficiency during translation (2'–deoxy or 2'–O–methyl; [89]). Modifications at 2'-hydroxyls of the codon also reduce tRNA binding affinity [26,88], EF-Tu GTPase activity [26],

translation fidelity [26] and translation efficiency [90]. These results are consistent with the role of these groups in stabilization of G530, A1492 and A1493.

Literature Cited

77 Engh, R. A. & Huber, R. Accurate bond and angle parameters for X-ray protein structure refinement. *Acta Cryst* **A47**, 392-400 (1991).

78 Saarma, U., Remme, J., Ehrenberg, M. & Bilgin, N. e. An A to U transversion at position 1067 of 23 S rRNA from Escherichia coli impairs EF-Tu and EF-G function1. *Journal of Molecular Biology* **272**, 327-335, doi:10.1006/jmbi.1997.1254 (1997).

79 Helm, M. Post-transcriptional nucleotide modification and alternative folding of RNA. *Nucleic Acids Research* **34**, 721-733, doi:10.1093/nar/gkj471 (2006).

80 Jackman, J. E. & Alfonzo, J. D. Transfer RNA modifications: nature's combinatorial chemistry playground. *Wiley Interdisciplinary Reviews: RNA* **4**, 35-48, doi:10.1002/wrna.1144 (2013).

81 Cabello-Villegas, J., Tworowska, I. & Nikonowicz, E. P. Metal Ion Stabilization of the U-Turn of the A37 N6-Dimethylallyl-Modified Anticodon Stem−Loop of Escherichia coli tRNAPhe. *Biochemistry* **43**, 55-66, doi:10.1021/bi0353676 (2004).

82 Cabello-Villegas, J., Winkler, M. E. & Nikonowicz, E. P. Solution Conformations of Unmodified and A37N6-dimethylallyl Modified Anticodon Stem-loops of Escherichia coli tRNAPhe. *Journal of Molecular Biology* **319**, 1015-1034, doi:10.1016/S0022-2836(02)00382-0 (2002).

83 Johansson, M., Zhang, J. & Ehrenberg, M. Genetic code translation displays a linear trade-off between efficiency and accuracy of tRNA selection. *PNAS* **109**, 131-136, doi:10.1073/pnas.1116480109 (2012).

84 Nierhaus, K. H. The allosteric three-site model for the ribosomal elongation cycle: features and future. *Biochemistry* **29**, 4997-5008, doi:10.1021/bi00473a001 (1990).

85 Blanchard, S. C., Kim, H. D., Gonzalez, R. L., Puglisi, J. D. & Chu, S. tRNA dynamics on the ribosome during translation. *PNAS* **101**, 12893-12898, doi:10.1073/pnas.0403884101 (2004).

86 Mittelstaet, J., Konevega, A. L. & Rodnina, M. V. Distortion of tRNA upon Near-cognate Codon Recognition on the Ribosome. *J. Biol. Chem.* **286**, 8158-8164, doi:10.1074/jbc.M110.210021 (2011).

87 Agirrezabala, X. *et al.* Structural Characterization of mRNA-tRNA Translocation Intermediates. *PNAS* **109**, 6094-6099, doi:10.1073/pnas.1201288109 (2012).

88 Fahlman, R. P., Olejniczak, M. & Uhlenbeck, O. C. Quantitative Analysis of Deoxynucleotide Substitutions in the Codon–Anticodon Helix. *Journal of Molecular Biology* **355**, 887-892, doi:10.1016/j.jmb.2005.11.011 (2006).

89 Satoh, A., Takai, K., Ouchi, R., Yokoyama, S. & Takaku, H. Effects of anticodon 2'-O-methylations on tRNA codon recognition in an Escherichia coli cell-free translation. *RNA* **6**, 680-686 (2000).

90 Hoernes, T. P. *et al.* Nucleotide modifications within bacterial messenger RNAs regulate their translation and are able to rewire the genetic code. *Nucleic Acids Research* **44**, 852-862, doi:10.1093/nar/gkv1182 (2016).